An enthalpy-based pyrolysis model for charring and non-charring materials in case of fire

Wasan, S.R.[1]; Rauwoens, P.[1]; Vierendeels; J.[1]; Merci, B.[1,2]

[1]Department of Flow, Heat and Combustion mechanics (IR03), Ghent University-UGent, Sint-Pietersnieuwstraat-41, B-9000 Ghent, Belgium

[2]Postdoctoral Fellow of the Fund of Scientific Research – Flanders (Belgium) (FWO-Vlaanderen)

Corresponding author: Bart.Merci@UGent.be

This paper is available online: **Article in Press,** Corrected Proof - Note to users

doi:10.1016/j.combustflame.2009.12.007 |

Abstract

In a simulation of a developing fire, flame spread must be properly accounted for. The pyrolysis model is important in this respect. To that purpose, we develop a simplified enthalpy based pyrolysis model that is extendable to multi-dimensional solid-phase treatments. This model is to be coupled to gas phase turbulent combustion simulations. The description of the pyrolysis process is simplified in order to acquire short simulation times. In this paper, first, the basic thermodynamic description of pyrolysis phenomena is revisited for charring and non-charring materials, possibly containing moisture. The heat of pyrolysis is defined and its relation to the formation enthalpies of individual constituents is explained. Solving only one equation for enthalpy on a fixed computational mesh, provides a useful description of the transport of heat and the pyrolysis process inside the solid material. Models for e.g. char oxidation or complex transport of the pyrolysis gases or water vapour inside the solid material can be coupled to the present model. Next, numerical issues and implementation are discussed. We consider basic test cases with imposed external heat flux to a solid material that can be dry or contain moisture. We illustrate that continuous pyrolysis gases mass flow rates are obtained when a piecewise linear representation of the temperature field is adopted on the fixed computational mesh. With constant temperature per computational cell, discontinuities, with sudden drops to zero, are encountered, as reported in the literature. We show that the present model formulation is robust with respect to numerical aspects (cell size and time step) and that the model performs well for variable external heat fluxes. For charring and non-charring materials, we validate the model results by means of numerical reference test cases and experimental data. By means of a numerical test case, we show that the model, when coupled to CFD calculations, is able to simulate flame spread.

Nomenclature

c	$specific\ heat, J/(kg.K)$
h	$specific\ enthalpy, J/kg$
k	$thermal\ conductivity, W/(m.K)$
m	$mass, kg$
$\dot{m}''$	$mass\ flux, kg/(m^2 s)$
L_v	$latent\ heat\ of\ evaporation\ of\ water, J/kg$
ΔQ_{pyr}	$heat\ of\ pyrolysis, J/kg$
$\dot{q}''$	$heat\ flux, (W/m^2)$
S	$volume\ boundary, m^2$
t	$time, s$
T	$temperature, K$
T_{pyr}	$pyrolysis\ front\ temperature, K$
V	$volume, m^3$
x	$coordinate\ direction, m$
y	$coordinate\ direction, m$
z	$coordinate\ direction, m$

Subscripts

c	$char$
$cond$	$conduction$
$conv$	$convection$
f	$front$
g	$(pyrolysis)\ gas$
i	$index$
ref	$reference$
v	$virgin$
v,dry	$dry\ virgin$
v,wet	$wet\ virgin$
w,l	$water\ (liquid)$
w,v	$water\ vapour$

Superscripts

o	$formation / initial\ value$
$*$	$shifted\ formation\ value$

Greek symbols

α	$mass\ fraction, kg/kg$
$\tilde{\rho}$	$local\ mass\ concentration, kg/m^3$
ρ	$bulk\ density, kg/m^3$

1 Introduction

In the development of a fire, flame spread always plays a very important role. In numerical simulations, this implies coupling of gas phase CFD ('Computational Fluid Dynamics') simulations, including turbulent combustion and radiation, to pyrolysis simulations in the solid material. In order to make such simulations possible, it is advantageous to keep the pyrolysis model simple.

During the past two decades, several researchers have developed numerical models for pyrolysis of charring materials, with different levels of complexity, such as: Arrhenius-type models [1]; 'integral' models [2-5]; an 'extended' integral model [6]; a moving mesh model [7]; a dual mesh model [8]. A review on pyrolysis modelling has recently been provided in [9]. For non-charring materials, it is common practice to work with a 'heat of gasification' at the pyrolysing surface and to consider a conduction problem in the solid materials (e.g. [2, 10-14]).

In the present paper, we describe in detail a simplified model, which is applicable to charring and non-charring materials, which can contain moisture. We also explain that the model is extendable for multi-dimensional solid-phase treatments, as required for general flame spread simulations. This is a difference to many existing simplified pyrolysis models, which might look very similar to the present model at first sight, but which are basically limited to one-dimensional configurations (or, at least, implementation for multi-dimensional solid-phase treatments becomes very cumbersome). Also, the present model can be combined with any model for the transport of gases or water vapour inside the solid material. In the same sense, e.g. a model for char oxidation can be added. We consider this beyond the scope of the present paper.

We deliberately avoid inclusion of pyrolysis kinetics. Whereas this limits the field of application to high-temperature pyrolysis and to situations where pyrolysis kinetics is not prevalent, it is relevant for flame spread situations as in a developing fire.

There are two major parts in the model description:

- the local relation between enthalpy and temperature;
- the energy equation to be solved in the solid material.

We first describe these parts in detail and define precisely what we mean by the 'heat of pyrolysis', in order to avoid any confusion on this term. Afterwards, we put our model and terminology in perspective with respect to existing models in the literature.

Next, numerical issues and implementation, including the solution procedure, are described in detail. An interesting feature of the model is the use of a fixed computational mesh.

Finally, we illustrate the accuracy of the results by means of a series of basic test cases. We discuss the following features:

- comparison to numerical reference results [5] and experimental data [15] for one-dimensional configurations in charring materials;
- the importance of the use of a piecewise linear approximation of the temperature field in the solid material for charring materials;
- sensitivity of the results with respect to the grid size and the time step;
- comparison to results [2] for PMMA;
- illustration that the model can deal with moisture in the solid;
- illustration that the model is applicable to multi-dimensional configurations, as required for general flame spread simulations.

The complete set of results aims at illustrating the robustness and accuracy of the simple model, with applicability to flame spread simulations in a developing fire.

2 Model description

2.1 Thermodynamics: Introduction

In our model, we focus on the thermodynamic description of the phenomena. Our approach is largely based on [16], one of the first theoretical papers on this topic. Below, we elaborate this to obtain an easy-to-use enthalpy-based pyrolysis model for three-dimensional simulations on a fixed computational mesh. The approach is to consider five constituents: virgin solid material, char, volatiles, liquid water and water vapour. In [16], the endothermic pyrolysis process is assumed to take place at a constant (pyrolysis) temperature T_{pyr}. At this temperature, the required energy to produce a mass unit of volatiles out of solid virgin material, for the pyrolysis process is denoted as $L(T_{pyr})$. In our notation, this is related to ΔQ_{pyr}. It is important to note that this energy is defined at temperature T_{pyr}. We come back to this point below.

In [17, 18], the same thermodynamic description for the enthalpy, in terms of temperature and local composition, is followed, in combination with Arrhenius type expressions to include pyrolysis process kinetics. The 'heat of reaction' L_g of those references corresponds to ΔQ_{pyr} below.

For charring materials, Atreya [19] and Sibulkin [20] report confusion on the notion and terminology of 'pyrolysis heat' (or 'heat of gasification') in the literature. Wide ranges of values are found in the literature for certain materials. For wood, e.g., values from 2.10^5J/kg up to 7.10^6J/kg are found [21-23]. As mentioned in [16-20], this is partly related to differences and/or a lack of precision in the definition, in particular at what temperature ΔQ_{pyr} is defined.

In [24], this concern is taken into consideration and the discussion on the heat of pyrolysis is described in terms of formation enthalpies. Below, we describe the relation between the

different approaches and explain how the need for knowledge on formation enthalpies is effectively avoided by the introduction of ΔQ_{pyr} into the model description.

For non-charring materials, there is no such confusion. There, it is very natural to define ΔQ_{pyr} at the surface temperature (equal to T_{pyr}), where the gasification process of the solid material is taking place. There is indeed a strong similarity to the vaporisation process of liquids (although the latter is in principle a reversible process in closed systems).

2.2 Thermodynamics: Relation between enthalpy and temperature

As mentioned in the introduction, an enthalpy based model approach is adopted to simulate the pyrolysis. The local relation between enthalpy and temperature is crucial.

We first describe the model in the most general manner. Afterwards, simplifications can readily be made (e.g. absence of moisture or char). As mentioned, we consider five constituents:

- (dry) virgin solid material (v);
- char (c);
- pyrolysis gases (g);
- water as a liquid ('moisture') (w,l);
- water vapour (w,v).

In fact, if desired, the pyrolysis gases can be further decomposed into different species in a mixture of volatiles, where each species is created at a different temperature. We do not go into this detail.

The five constituents do not all co-exist. At atmospheric pressure, e.g., we assume that liquid water only exists if $T < 373K$, whereas water vapour only exists when $T > 373K$. Also, virgin solid material and char cannot co-exist.

As in [16], we model pyrolysis as an infinitely fast, irreversible, endothermic and isothermal process, taking place at the 'pyrolysis temperature' T_{pyr}, which is a model parameter. As such,

reaction kinetics are not considered and the pyrolysis zone becomes infinitely thin ('pyrolysis front'). This assumption makes the model particularly appealing due to its simplicity to couple to gas phase combustion CFD simulations (e.g. for flame spread simulations). Note that virgin solid material now only exists as long as $T < T_{pyr}$.

The specific enthalpy at position *(x,y,z)* at time *t* can be expressed as a mass-weighted sum of the specific enthalpies of the constituents, present at *(x,y,z)* at that time. Thus, the specific enthalpy at any time and any position can be written as:

$$h(x,y,z,t) = \sum_i \alpha_i(x,y,z,t) h_i\left(T_i(x,y,z,t)\right) \qquad (1)$$

with $\alpha_i(x,y,z,t) = \tilde{\rho}_i(x,y,z,t) / \tilde{\rho}(x,y,z,t)$ and $\tilde{\rho}(x,y,z,t) = \sum_i \tilde{\rho}_i(x,y,z,t)$. Thus α_i(x,y,z,t) is the local mass fraction of constituent *i* and $\tilde{\rho}_i(x,y,z,t)$ denotes the local mass concentration of this constituent. We assume that the specific enthalpy of each constituent is only dependent on the temperature.

If a constituent is not present at *(x,y,z,t)*, the mass fraction of that constituent is equal to zero in (1). If char or virgin is present, $\tilde{\rho}_c = \rho_c$ and $\tilde{\rho}_v = \rho_v$: the local mass concentration equals the bulk density of that constituent. If transport of moisture is not considered and the initial moisture distribution is uniform, $\tilde{\rho}_{w,l} = \rho_{w,l}$ at positions where moisture is present. This corresponds to the 'moisture bulk density'.

In principle, the local temperature of each constituent can be different, but here we assume that there is locally a thermal equilibrium, so that, from now on, *T(x,y,z,t)* will be used as the local temperature for all constituents ($T_i(x,y,z,t) = T(x,y,z,t)$ for all *i*). With this assumption, only one energy equation has to be solved to compute the temperature distribution. For ease of notation, *(x,y,z,t)* is omitted from now on.

For each of the five constituents, the relation between enthalpy and temperature reads:

$$h_i(T) = h_i^o(T_{ref}) + \int_{T_{ref}}^{T} c_i(T)\,dT\,. \qquad (2)$$

The total specific enthalpy is indeed the sum of the formation enthalpy at a reference temperature T_{ref} (typically chosen as 298K) and the thermal enthalpy. For gases and water vapour, the thermal capacity at constant pressure is used.

In principle, equations (1) and (2) completely define the relation between the specific enthalpy and the temperature, when the local composition of the material is known. Some difficulties arise, though. First of all, the exact composition of the pyrolysis gases is typically not known, which makes it effectively impossible to evaluate relation (2) for the volatiles. Even more so, the necessity of this exact knowledge is deliberately avoided in (simplified) modelling. Also, the formation enthalpies of the virgin solid material and char (when present) are not known. On the other hand, the concept of 'heat of pyrolysis' can be introduced, providing a relation between the individual enthalpies (2). As explained below, introduction of ΔQ_{pyr} allows circumventing the necessity of the complete knowledge of all formation enthalpies and the exact gas composition. Modelling pyrolysis as an isothermal process at $T = T_{pyr}$, an amount of mass (m_v) of solid virgin material is transformed into an amount of mass (m_c) char and an amount of mass (m_v-m_c) pyrolysis gases, all at $T = T_{pyr}$. This endothermic process requires an amount of energy equal to $(m_v\text{-}m_c)\Delta Q_{pyr}$. It is important to point out that, as in [16-18], we define the heat of pyrolysis as the amount of energy required to produce a unit mass of volatiles out of solid dry virgin material, at $T = T_{pyr}$. The relation then reads:

$$m_v h_v(T_{pyr}) + (m_v - m_c)\Delta Q_{pyr} = m_c h_c(T_{pyr}) + (m_v - m_c) h_g(T_{pyr}) \qquad (3)$$

Taking the limit to an infinitesimally small volume at (x,y,z), this can be rewritten in terms of bulk densities:

$$h_v(T_{pyr}) + \left(1 - \frac{\rho_c}{\rho_v}\right)\Delta Q_{pyr} = \frac{\rho_c}{\rho_v} h_c(T_{pyr}) + \left(1 - \frac{\rho_c}{\rho_v}\right) h_g(T_{pyr}) \qquad (4)$$

In words, expression (3) reads: the sum of the enthalpies of char and pyrolysis gases at T_{pyr} is $(m_v - m_c)\Delta Q_{pyr}$ higher than the enthalpy of virgin solid material at that temperature. This equation determines ΔQ_{pyr}, but, as mentioned above, since the constitution of the virgin material, the char material and the pyrolysis gases is typically not exactly known, their formation enthalpies are unknown. On the other hand, only enthalpy differences are important. Thus, a shift Δh_i can be applied for each constituent:

$$h_i(T) = h_i^o(T_{ref}) + \Delta h_i + \int_{T_{ref}}^{T} c_i(T)\,dT \quad \text{or} \quad h_i(T) = h_i^*(T_{ref}) + \int_{T_{ref}}^{T} c_i(T)\,dT \,. \tag{5}$$

with $h_i^*(T_{ref}) = h_i^o(T_{ref}) + \Delta h_i$. Prescribing the heat of pyrolysis ΔQ_{pyr}, fulfilment of equation (4) implies that the shifts Δh_i for the virgin, char and pyrolysis gases cannot all be chosen independently. Indeed, only two constants can be chosen freely, while the third one is determined by eq. (4). We come back to the discussion of formation enthalpies in the next section.

From now on, $h_v^*(T_{pyr})$ and $h_g^*(T_{pyr})$ are chosen equal to zero for charring materials. Because of (4) and (5), this results in:

$$h_v(T) = \int_{T_{pyr}}^{T} c_v(T)\,dT,\ h_g(T) = \int_{T_{pyr}}^{T} c_g(T)\,dT, h_c(T) = \left(\frac{\rho_v}{\rho_c} - 1\right)\Delta Q_{pyr} + \int_{T_{pyr}}^{T} c_c(T)\,dT \,. \tag{6}$$

Another choice should be made for non-charring materials $(\rho_c = 0)$. Then only 2 constituents exist and only one constant can be chosen. If, again, $h_v^*(T_{pyr})$ is chosen equal to zero, the enthalpy of virgin material and volatiles as a function of temperature is given by:

$$h_v(T) = \int_{T_{pyr}}^{T} c_v(T)\,dT,\ h_g(T) = \Delta Q_{pyr} + \int_{T_{pyr}}^{T} c_g(T)\,dT \,. \tag{7}$$

Possible presence of moisture does not affect the balance (4), as pyrolysis takes place at $T_{pyr} > 373K$ and water vapour does not affect the thermodynamics of the pyrolysis process.

Obviously, when there is moisture in the virgin material, evaporation must be accounted for. This process takes place at *373K* and the latent heat L_v is defined by

$$\left(h_{w,l}^{o} + \int_{T_{ref}}^{373} c_{w,l}\left(T\right) dT \right) + L_v = \left(h_{w,v}^{o} + \int_{T_{ref}}^{373} c_{w,v}\left(T\right) dT \right). \qquad (8)$$

With expression (5) for the specific enthalpy, applied to the water liquid and water vapour, it is clear from eq. (8) that, if the specific enthalpy of the liquid water is shifted, the same shift should be made in the specific enthalpy of the water vapour and vice versa. In this paper, we take $h_{w.l}^{*}\left(T_{ref}\right)$=0, with T_{ref} = 298K. This results in:

$$\begin{aligned} h_{w,l}\left(T\right) &= \int_{T_{ref}}^{T} c_{w,l}\left(T\right) dT, \quad if\ T < 373K \\ h_{w,v}\left(T\right) &= \int_{T_{ref}}^{373} c_{w,l}\left(T\right) dT + L_v + \int_{373}^{T} c_{w,v}\left(T\right) dT, \quad if\ T > 373K \end{aligned} \qquad (9)$$

Figure 1 summarises the expressions above for charring and non-charring materials. For ease of drawing, constant thermal capacities are assumed.

With expressions (1), (6) or (7) and (9), we can now define the local relations between the specific enthalpy and the temperature for the different temperature ranges:

a. $T > T_{pyr}$

This is only possible in charring materials. Under this condition, only char, pyrolysis gases and water vapour can be present. Expression (1) then reads:

$$h\left(T\right) = \alpha_c h_c\left(T\right) + \alpha_g h_g\left(T\right) + \alpha_{w,v} h_{w,v}\left(T\right) \qquad (10.1)$$

b. $373K < T < T_{pyr}$

For charring materials, there are two possibilities for the local composition:

- char + gases + water vapour (during a cooling phase after pyrolysis): expression (10.1);
- virgin + water vapour. In this case, the expression becomes:

$$h\left(T\right) = \alpha_v h_v\left(T\right) + \alpha_{w,v} h_{w,v}\left(T\right) \qquad (10.2)$$

For non-charring materials, only expression (10.2) is possible.

c. T < 373K

For charring materials, there are again two possibilities for the local composition:

- char + gases (during a cooling phase after pyrolysis):

$$h(T) = \alpha_c h_c(T) + \alpha_g h_g(T) + \alpha_{w,l} h_{w,l}(T) \quad (10.3)$$

If condensation is accounted for, a term with liquid water must be added. We do not consider condensation in the present study.

- virgin + liquid water. In this case, the expression becomes:

$$h(T) = \alpha_v h_v(T) + \alpha_{w,l} h_{w,l}(T) \quad (10.4)$$

For non-charring materials, only expression (10.4) is possible.

If it is assumed that water vapour and pyrolysis gases leave the solid as soon as they are generated, $\alpha_g = \alpha_{w,v} = 0$ in the expressions above.

2.3 Formation enthalpies: discussion

In the previous section, we illustrated a direct link between the formation enthalpies of the different constituents and the 'heat of gasification' or 'heat of pyrolysis'. The lack of precision in the definitions seems to be an important source of confusion in terminology in the literature. Indeed, starting from the basic expression (2), it becomes clear how ΔQ_{pyr} depends on the temperature where it is defined. In fact, this is seen in expression (4): if one knew the exact composition, thermal capacities at all temperatures and standard formation enthalpies of all constituents, ΔQ_{pyr} can be computed as function of T_{pyr}. This also shows that ΔQ_{pyr} is not a model parameter to be chosen freely. In [24], it is in fact described how ΔQ_{pyr} can be computed from the formation enthalpies of virgin material, char and volatiles. However, as mentioned before, one typically does not dispose of the knowledge, required to

compute ΔQ_{pyr}. Rather, one uses the notion of ΔQ_{pyr} in order to avoid the necessity to have this complete knowledge. Prescription of ΔQ_{pyr} then leads to expressions like (6) or (7). Indeed, only enthalpy differences are of importance, so one has the liberty to choose e.g. $h_v^* = 0$, without loss of generality in the pyrolysis model. In fact, this is implicitly done in e.g. [16-18]. In [17, 18, 24] the discussion on formation enthalpy is avoided by discussion of time derivatives of enthalpy. This is equivalent to stating that only enthalpy differences need to be considered and the formation enthalpy of virgin material can be chosen equal to zero.

The discussion is similar for the water vaporisation process, which is considered independent of the pyrolysis process. We do not consider condensation here.

2.4 Model description - Enthalpy equation

In our model, the solid material is divided into a number of control volumes, which are kept fixed during the simulations (fixed computational mesh). In fact, it is a particularly appealing feature of the present model that the equations are solved on a fixed computational mesh. Provided that a piecewise linear temperature field is used, this mesh need not be extremely fine and time steps in the solution procedure for the enthalpy equation need not be extremely small [15]. This allows the model to be used for multi-dimensional solid-phase treatments, which becomes far more cumbersome with intrinsically one-dimensional pyrolysis models, such as integral type models [2-5], or with moving mesh [7] or dual mesh [8] models. Discretisation issues and a sensitivity study are discussed below. In the present section, we only describe the equations to be solved. We describe the model in finite volume formulation, as this is used in the solution procedure. For information purposes, the PDE formulation is described in appendix A.

For a fixed (sub-)volume 'V', the energy equation reads:

$$\frac{\partial}{\partial t}\int_V \tilde{\rho} h dV = -\int_S \vec{\dot{q}}'' \cdot \vec{n}\, dS \qquad (11)$$

with $\vec{\dot{q}}'' \cdot \vec{n}$ the heat flux out of the volume '*V*' through its boundary *S*, as $\vec{n}$ is the unit normal vector, pointing outward with respect to the volume. Note that, in principle, the specific internal energy should be used on the left hand side of equation (11). In the solid material, though, we ignore the (thermodynamic) effect from static pressure. Therefore, we use 'enthalpy' from now on. We also assume that there will be no accumulation of water vapour or pyrolysis gases inside the material, so that $\tilde{\rho}_g = \tilde{\rho}_{w.v} = 0$ inside the material. Note that $\tilde{\rho}_g = \tilde{\rho}_{w.v} = 0$ does not imply that there are no convective fluxes related to these constituents (see below). In a more general approach, one can work with specific internal energy and accumulation of pyrolysis gases, water vapour and water liquid. Then a mass balance equation for each constituent is required and if the velocity field for some of these constituents has to be determined as well, also a momentum equation is needed for those constituents.

2.4.1 Heat fluxes through the volume boundaries

The right hand side of equation (11) consists of conduction and convection heat fluxes, i.e.:

$$\vec{\dot{q}}'' = \vec{\dot{q}}''_{cond} + \vec{\dot{q}}''_{conv} \qquad (12)$$

Conduction is modelled by Fourier's law:

$$\vec{\dot{q}}''_{cond} = -k\nabla T \qquad (13)$$

The local thermal conductivity is used. The value might depend on temperature and local composition at the cell face. In principle, the effect of the presence of pores in the char needs to be taken into account. In these pores, conduction in the gas phase can take place, possibly in combination with natural convection and, at sufficiently high temperatures, radiation. Such effects are not explicitly included in our model, i.e. we simply use $k = k_c$ in the char. This is exact in the limit of zero porosity and is an approximation in the case of non-zero porosity.

The convective fluxes due to transport of pyrolysis gases and water vapour (and possibly water liquid) are given by:

$$\vec{\dot{q}}''_{conv} . \vec{n} = \dot{m}''_g h_g (T) + \dot{m}''_{w,v} h_{w,v} (T) + \dot{m}''_{w,l} h_{w,l} (T) \qquad (14)$$

$\dot{m}''_i$ denotes the mass flux (kg/m^{2}s) of constituent *i* leaving the volume, as determined below. The specific enthalpies are computed from (6) or (7) and (9).

2.4.2 Motion of pyrolysis and evaporation front

For charring materials, the motion of the pyrolysis front (at $T = T_{pyr}$) is determined from a local energy and mass balance at the front (shown for a one-dimensional configuration in Figure 2). This boils down to expressing that the net conductive heat flux to the front (i.e. the difference between incoming and outgoing conductive heat fluxes) is used to provide the heat of pyrolysis per unit of time for the pyrolysis process:

$$(\rho_v - \rho_c) v_{f,pyr} \Delta Q_{pyr} = -k_c \nabla T|_c + k_v \nabla T|_v . \qquad (15)$$

with $v_{f,pyr}$ the pyrolysis front velocity in the direction normal to the front, from the char towards the virgin material. Note that no convection term from the pyrolysis gases appears explicitly in eq. (15), as they leave the pyrolysis front at temperature T = T_{pyr} and this phenomenon is taken into account by the definition of ΔQ_{pyr} as described above (see, e.g., eq. (3)). The local balance at the front indeed reveals that virgin material becomes a combination of char and pyrolysis gases, all at T = T_{pyr}.

The mass of gases, produced per unit of time and per unit of pyrolysis front area, is also related to the motion of the pyrolysis front through the mass balance:

$$\dot{m}''_g = (\rho_v - \rho_c) v_{f,pyr} \qquad (16)$$

Thus, expression (15) determines the pyrolysis front motion. It is important to note that a motion of the front requires an amount of energy. This is reflected in the relation between the enthalpy in a cell and the local composition and temperature field (see section 2.2). Note that,

when there is no pyrolysis, e.g. in a cooling phase, expression (15) merely relates the temperature derivatives to the local thermal conductivities (change of material type over the pyrolysis front).

For non-charring materials, the conduction term in the char in expression (15) is replaced by the incident heat flux onto the solid material surface and ρ_c is equal to zero in (16) (conservation of mass).

At *T = 373K*, the following expression gives the motion of the evaporation front:

$$\dot{m}_w'' L_v = -k_{v,dry} \nabla T\big|_{v,dry} + k_{v,wet} \nabla T\big|_{v,wet} \qquad (17)$$

The subscript *v,dry* stands for 'dry virgin'. This is the same as the solid virgin material mentioned above. On the other hand, *v,wet* means 'wet virgin', i.e. the solid virgin material, containing an amount of water. This is merely important in the determination of the conductivity (conduction through water vapour and pyrolysis gases are ignored). $\dot{m}_w''$ denotes the mass of water that evaporates per unit of time and unit of area of the evaporation front, equal to $\dot{m}_w'' = \tilde{\rho}_{w,l} v_{f,evap}$, where $v_{f,evap}$ is the evaporation front velocity in the direction normal to the front, from the dry virgin towards the wet virgin material.

Expression (17) is valid for charring and non-charring materials. As mentioned above, the mass concentration of liquid water, $\tilde{\rho}_{w,l}$, can be computed from transport equations. As mentioned earlier, if no transport of the liquid water is taken into account and the initial moisture distribution is uniform, the mass concentration of liquid water in the virgin wet material equals the initial 'moisture bulk density' $\rho_{w,l} = \rho^o_{v,wet} - \rho^o_{v,dry}$, which can be computed from the initial values of the bulk densities of the virgin wet $\rho^o_{v,wet}$ and the virgin dry material $\rho^o_{v,dry} = \rho_v$.

If no water vapour is accumulated in the solid material, $\tilde{\rho}_{w,v}$ is zero at all times and only evaporation can take place. When in such a case the evaporation front temperature drops below 373K, the position of the front is kept fixed, $\dot{m}''_w$ becomes equal to zero and eq. (17) gives a relation between the temperature gradients at each side of the front.

2.5 Discussion: Relation with existing pyrolysis models

The theoretical concepts, elaborated above from basic thermodynamic principles, have already been described in e.g. [16, 17, 24]. We revisited the derivation and the relation between 'heat of pyrolysis' and formation enthalpies, considering 5 constituents. As such, this theoretical concept is not new. The novelty in the present work, though, is that a model has been developed that:

a) is applicable to charring and non-charring materials;
b) is applicable to materials with moisture content;
c) is applicable in three dimensions;
d) does not rely on any assumptions on temperature fields;
e) is easy to implement, using a fixed computational mesh;
f) is relatively cheap in terms of computing times;
g) readily and correctly deals with transient phenomena (e.g. in imposed heat flux);
h) can be combined with any transport model for gases, liquid water and water vapour.

Application of the model is illustrated below. It is useful, though, to already put the present model into perspective with respect to existing pyrolysis models.

For non-charring materials, the model boils down to the use of a 'heat of gasification' at the pyrolysing surface, at $T = T_{pyr}$. This notion is also used in e.g. [10-13]. The calculation then consists of solving a conduction problem, with an incoming heat flux and a moving boundary as the pyrolysis takes place. Note that no moving mesh is required: it suffices to compute the front motion as described above and temperatures need not be computed in regions where

there is no material left. Also, the problem can be three-dimensional, in contrast to integral type models [2-6, 12] or models where essentially one-dimensional configurations are assumed [9]. Thus, our model is applicable to flame spread over thermally thick and thermally thin materials.

This is also true for charring materials (no moving mesh [7] or dual mesh [8] is required for the solution of the equations, and the applicability in three dimensions is an interesting advantage over 'integral type' models [2-6]).

Admittedly, pyrolysis kinetics is deliberately not taken into account. This implies a limitation in applicability to situations where sharp fronts provide a good approximation for the pyrolysis and evaporation processes. Note however, that multiple fronts (at different temperatures) can easily be introduced, so that the pyrolysis process could be modeled by means of several fronts. At each front, a species of the pyrolysis gas mixture is then generated. Note that also a char oxidation front can be introduced this way. Obviously, transport of oxygen must be considered then, but this is no problem with the present model, which can be combined with any transport model for any species.

Finally, we recall that the model readily deals with any transient imposed heat fluxes onto the solid material, as illustrated below. This means that coupling to CFD packages is relatively straightforward. The heat flux onto the solid material is then obtained from the gas phase CFD calculations, while the present model gives mass flow rates and temperatures as boundary conditions to the CFD package. In this context, we mention that in e.g. FDS, version 5, Arrhenius expressions are used but, more importantly, the equation in the solid material is essentially one-dimensional. This is thus a limitation of that model.

3. Implementation and solution procedure

As described in the previous section, the model considers enthalpy as the basic variable, for which a transport equation is solved. We are, however, not interested in enthalpy itself, but

rather in temperature distribution and volatile production. The latter is related to the motion of the pyrolysis front, which is assumed infinitely thin in the present model formulation. So, we require a procedure to reconstruct temperature and front position from the basic enthalpy variable. This is done, using the relationships between these variables, as described above.

We recall that pyrolysis is treated as an endothermic process, taking place infinitely fast at $T = T_{pyr}$, which effectively reduces the pyrolysis region to an infinitely thin front. The same is true for the evaporation process, being infinitely fast at $T = T_{evap}$. Some further assumptions are made in the applications below: we assume that water vapour and pyrolysis gases leave the solid material at the side of the imposed external heat flux as soon as they are generated. This is the simplest possible transport model. The vapour and volatiles are further assumed to take the local temperature of the solid material (local thermal equilibrium throughout the solid). These sub-models can be refined, but we consider this beyond the scope of the present paper.

3.1 Solution procedure

The flow chart in Figure 3 illustrates the solution procedure for dry charring materials. The treatment of the vaporisation front (at $T = 373K$) is similar to the treatment of the pyrolysis front and will therefore not be discussed.

Starting from the initial conditions, physical time steps $\Delta t = t^{n+1} - t^n$ are taken until the end of the simulation. From the most recent situation, the conduction and convection fluxes are computed first for the enthalpy equation to be solved for each computational cell. Stepping from time t^n to t^{n+1} occurs in an iterative manner. We denote the pseudo-time levels, for the evolution from t^n to t^{n+1} as $t^{n+1,k}$ or $t^{n+1,k+1}$, where the index k or $k+1$ indicates what values are used within this iterative procedure. From the fluxes, the enthalpy update is computed:

$$\left(\tilde{\rho}h\right)_i^{n+1,k+1} = \left(\tilde{\rho}h\right)_i^{n} + \frac{\Delta t}{\Delta x_i}\left[\left(\dot{q}''^{n+1,k+1}_{cond,i-½} - \dot{q}''^{n+1,k+1}_{cond,i+½}\right) + \left(\dot{q}''^{n+1,k}_{conv,i-½} - \dot{q}''^{n+1,k}_{conv,i+½}\right)\right] \qquad (18)$$

In (18), $\tilde{\rho} = \sum_i \tilde{\rho}_i$, the local mass concentration (see above).

In fact, only the central node is treated point-implicitly in the conductive fluxes in the sub-iterations described below. From the new enthalpy field, the temperature field, the position of the pyrolysis front and the pyrolysis front temperature must be reconstructed. As long as no pyrolysis process is taking place, only the temperature field must be reconstructed. Here, we describe what must be done when there is a pyrolysis front.

If the pyrolysis process is ongoing, the pyrolysis front temperature is constant, equal to $T_f^{n+1,k+1} = T_f^{n+1,k} = T_{pyr}$. Thus, if $T_f^{n+1,k} = T_{pyr}$, the enthalpy update leads to a new temperature field $T_i^{n+1,k+1}$ and a movement of the pyrolysis front to a new position $x_f^{n+1,k+1}$. The front is allowed to move backwards during the iterative procedure, but it must not move back to a position $x_f^{n+1,k+1} < x_f^n$, as pyrolysis is an irreversible process. Thus, we check this. If $x_f^{n+1,k+1} \geq x_f^n$, there is no problem and we check convergence of the iterative procedure. This is done by means of an 'L_∞' residual $res = \log\left(\max_i\left(\left|res_i\right|\right)\right)$, where res_i is defined for each cell as: $res_i = -\frac{\left(\tilde{\rho}h\right)_i^{n+1,k} - \left(\tilde{\rho}h\right)_i^n}{\Delta t} + \frac{\dot{q}''^{,n+1,k}_{i-1/2} - \dot{q}''^{,n+1,k}_{i+1/2}}{\Delta x_i}$. We compare with the residual for *k = 0* and assume convergence when the residual dropped 5 orders of magnitude. If the convergence criterion is met, the next time level *n+1* is achieved. If not, we go to the next iteration.

We now describe what happens if any of the above mentioned tests is 'not true'. First, it is possible that $T_f^{n+1,k} < T_{pyr}$, which means that previously, there has already been pyrolysis, but the pyrolysis process stopped (e.g. due to insufficient incoming heat flux for the pyrolysis process to continue). Then the pyrolysis front does not move and the new temperature field $T_i^{n+1,k+1}$ and the new pyrolysis front temperature $T_f^{n+1,k+1}$ are computed from the new enthalpy

field. In the case of heating, it is possible that $T_f^{n+1,k+1} > T_{pyr}$. On the other hand, in our model the front temperature cannot exceed T_{pyr}. Thus, if $T_f^{n+1,k+1} > T_{pyr}$ is true, we clip the front temperature to $T_f^{n+1,k+1} = T_{pyr}$ and go to the next iteration. In this next iteration, the test $T_f^{n+1,k} = T_{pyr}$ will be true and the pyrolysis front will be allowed to move. Thus, it is possible that, within one physical time step from t^n to t^{n+1}, the pyrolysis front heats up to T_{pyr} and moves.

The second test fails if $x_f^{n+1,k+1} < x_f^n$. If so, we clip the front position to $x_f^{n+1,k+1} = x_f^n$ and we must compute the front temperature. Indeed, if the solution for the front position were a backward motion due to the enthalpy update, this is prohibited and cooling of the pyrolysis front is computed instead. From that point onwards, we proceed as just described.

3.2 Conductive fluxes

The conductive fluxes of cell faces are calculated using Fourier's law:

$$\dot{q}''_{cond,i\pm1/2} = -k_{i\pm1/2} \left.\frac{dT}{dx}\right|_{r/l,i} \tag{19}$$

As mentioned, the local material properties are used: $k_{i\pm1/2} = k_c$ if face *i±1/2* is in char material and $k_{i\pm1/2} = \alpha_v k_v + \alpha_{w,l} k_{w,l}$ if it is in virgin material, with α_i the local mass fraction of constituent *i*. Thus, e.g. $k_{i\pm1/2} = k_v$ if the face is in dry virgin material. For the temperature derivatives, a piecewise linear representation of the temperature field is used. It is explained in section 4 that a piecewise linear representation is necessary to predict a continuous mass flow rate of volatile gases. Figure 4 illustrates the temperature function for temperatures stored in the cell centres. If there is no front in the cell, a straight line connects two neighbouring temperatures. If a front is present between two cell centres, the linearity is broken into two parts: linear from cell centre *i* to the front, and again linear from the front to cell centre *i+1*.

3.3 Convective fluxes

Equation (18) shows that the fluxes through the cell faces determine the update in enthalpy of the cell. Besides heat transfer by means of conduction, energy is also transported with the movement of water vapour and volatiles out of the solid material. The water vapour and volatiles are assumed to be everywhere in local thermal equilibrium with the solid material through which they flow, as they absorb heat. We assume that there is no accumulation of volatiles or vapour in the solid material. The convective flux through cell face *i-1/2* reads:

$$\dot{q}''^{n+1,k}_{conv,i-1/2} = -\dot{m}''^{n+1,k}_{w,v,i-1/2} \cdot h_{w,v}\left(T^{n+1,k}_{i-1/2}\right) - \dot{m}''^{n+1,k}_{pyr,i-1/2} \cdot h_g\left(T^{n+1,k}_{i-1/2}\right). \qquad (20)$$

We recall that $h_{w,v}(T) = c_{w,v}\left(T - T_{evap}\right)$ and, for a charring material, $h_g(T) = c_g\left(T - T_{pyr}\right)$.

The mass flow rates are determined as:

$$\dot{m}''^{n+1,k}_{pyr,i-1/2} = \sum_{j=i}^{N} (\rho_v - \rho_c) \frac{\left(\xi_j^{n+1,k} - \xi_j^{n}\right)}{\Delta t} \Delta x_j \quad \xi_i^{n+1,k+1} = \min\left(\max\left(0, \frac{x_f^{n+1,k+1} - x_{i-1/2}}{\Delta x_i}\right), 1\right)$$
$$\dot{m}''^{n+1,k}_{w,v,i-1/2} = \sum_{j=i}^{N} \tilde{\rho}_{w,l} \frac{\left(\xi_{w,j}^{n+1,k} - \xi_{w,j}^{n}\right)}{\Delta t} \Delta x_j \quad , \quad \xi_{w,i}^{n+1,k+1} = \min\left(\max\left(0, \frac{x_{f,evap}^{n+1,k+1} - x_{i-1/2}}{\Delta x_i}\right), 1\right) \qquad (21)$$

The cell face temperatures are computed, using the piecewise linear representation of the temperature. Also note that we only consider uni-directional flow of the pyrolysis gases towards the side where the external heat flux is imposed. The model could be extended to account for other mass fluxes, but this is not relevant for the present study.

3.4 Reconstruction of temperature field and fronts' position

From equation (18), the enthalpy update can be calculated. For the construction of the fluxes, the knowledge of the temperature and fronts' position is needed, though. Therefore, from the updated enthalpy values, the temperature field and fronts' position must be reconstructed. Two constraints determine the relation between these variables: the enthalpy is a function of

temperature and local composition and the motion of the front correlates the temperature gradients on both sides of the fronts.

3.4.1 Constraint 1: enthalpy as a function of temperature and composition

We introduce a function $F_{enth,i}$, for each computational cell, to express the relationship between the enthalpy value and the temperature. This relates to expressions (10). As we assume here that water vapour and volatiles leave the solid material as soon as they are formed, the mass fractions $\alpha_{w,v}$ and α_g are zero.

We consider the value for enthalpy as the averaged value over the computational cell. For a one-dimensional configuration, this reads:

$$\left(\tilde{\rho}h\right)_i \Delta x_i = \int_{x_{i-1/2}}^{x_{i+1/2}} \sum_k \tilde{\rho}_k\left(x\right) h_k\left(T\left(x\right)\right) \cdot dx \qquad (22)$$

where $T\left(x\right)$ is the piecewise linear temperature distribution. The local mass concentration of the components is a piecewise constant function, whose value depends on the fronts position. As such, a few possible configurations can be distinguished, for which different expressions can be formulated, all derived from the general form:

$$F_{enth,i}\left(T_i,\left(\tilde{\rho}h\right)_i, x_f, T_f, x_{f,evap}, T_{f,evap}\right) \triangleq \int_{x_{i-1/2}}^{x_{i+1/2}} \sum_k \tilde{\rho}_k\left(x\right) h_k\left(T\left(x\right)\right) \cdot dx - \left(\tilde{\rho}h\right)_i \Delta x_i = 0 \quad (23)$$

We distinguish between the following possible cell configurations. The following expressions are valid for charring and non-charring materials. In the latter, ρ_c must simply be set to zero.

a. Cell *i* is char (only relevant in charring materials):

$$\begin{aligned} F_{enth,i}\left(T_i,\left(\tilde{\rho}h\right)_i\right) = {} & \frac{x_i - x_{i-1/2}}{2}\left[\rho_c c_c\left(T_i - \frac{1}{4}\Delta x_i \left.\frac{dT}{dx}\right|_{l,i} - T_{pyr}\right) + \left(\rho_v - \rho_c\right)\Delta Q_{pyr}\right] \\ & + \frac{x_{i+1/2} - x_i}{2}\left[\rho_c c_c\left(T_i + \frac{1}{4}\Delta x_i \left.\frac{dT}{dx}\right|_{r,i} - T_{pyr}\right) + \left(\rho_v - \rho_c\right)\Delta Q_{pyr}\right] \\ & - \left(\tilde{\rho}h\right)_i \Delta x_i \end{aligned} \qquad (23a)$$

b. Cell *i* contains the pyrolysis front:

$$x_f \le x_i : F_{enth,i}\left(T_i,(\tilde{\rho}h)_i,x_f,T_f\right)=(x_f-x_{i-1/2})\left[\rho_c c_c\left(T_f-\frac{x_f-x_{i-1/2}}{2}\frac{dT}{dx}\Big|_{l,i}-T_{pyr}\right)+\left(\rho_v-\rho_c\right)\Delta Q_{pyr}\right]$$
$$+(x_i-x_f)\left[\rho_v c_v\left(\frac{T_f+T_i}{2}-T_{pyr}\right)\right]$$
$$+(x_{i+1/2}-x_i)\left[\rho_v c_v\left(T_i+\frac{\Delta x}{4}\frac{dT}{dx}\Big|_{r,i}-T_{pyr}\right)\right] \quad (23b)$$
$$-\left(\tilde{\rho}h\right)_i\Delta x_i$$

$$x_f > x_i : F_{enth,i}\left(T_i,(\tilde{\rho}h)_i,x_f,T_f\right)=(x_i-x_{i-1/2})\left[\rho_c c_c\left(T_i-\frac{\Delta x}{2}\frac{dT}{dx}\Big|_{l,i}-T_{pyr}\right)+\left(\rho_v-\rho_c\right)\Delta Q_{pyr}\right]$$
$$+(x_f-x_i)\left[\rho_c c_c\left(\frac{T_f+T_i}{2}-T_{pyr}\right)+\left(\rho_v-\rho_c\right)\Delta Q_{pyr}\right]$$
$$+(x_{i+1/2}-x_f)\left[\rho_v c_v\left(T_f+\frac{x_{i+1/2}-x_f}{2}\frac{dT}{dx}\Big|_{r,i}-T_{pyr}\right)\right]$$
$$-\left(\tilde{\rho}h\right)_i\Delta x_i$$

c. Cell *i* is virgin dry material and does not contain a front:

$$F_{enth,i}\left(T_i,(\tilde{\rho}h)_i\right)=\frac{x_i-x_{i-1/2}}{2}\left[\rho_v c_v\left(T_i-\frac{1}{4}\Delta x_i\frac{dT}{dx}\Big|_{l,i}-T_{pyr}\right)\right]$$
$$+\frac{x_{i+1/2}-x_i}{2}\left[\rho_v c_v\left(T_i+\frac{1}{4}\Delta x_i\frac{dT}{dx}\Big|_{r,i}-T_{pyr}\right)\right] \quad (23c)$$
$$-\left(\tilde{\rho}h\right)_i\Delta x_i$$

d. Cell *i* contains the evaporation front:

$$x_{f,evap} \le x_i : F_{enth,i}\left(T_i,(\tilde{\rho}h)_i,x_{f,evap},T_{f,evap}\right)=(x_{f,evap}-x_{i-1/2})\left[\rho_v c_v\left(T_{f,evap}-\frac{x_f-x_{i-1/2}}{2}\frac{dT}{dx}\Big|_{l,i}-T_{pyr}\right)\right]$$
$$+(x_i-x_{f,evap})\left[\rho_v c_v\left(\frac{T_{f,evap}+T_i}{2}-T_{pyr}\right)\right]$$
$$+(x_{i+1/2}-x_i)\left[\rho_v c_v\left(T_i+\frac{\Delta x}{4}\frac{dT}{dx}\Big|_{r,i}-T_{pyr}\right)\right] \quad (23d)$$
$$+(x_i-x_{f,evap})\left[\rho_{w,l} c_{w,l}\left(\frac{T_{f,evap}+T_i}{2}-T_{ref}\right)\right]$$
$$+(x_{i+1/2}-x_i)\left[\rho_{w,l} c_{w,l}\left(T_i+\frac{\Delta x}{4}\frac{dT}{dx}\Big|_{r,i}-T_{ref}\right)\right]$$
$$-\left(\tilde{\rho}h\right)_i\Delta x_i$$

$$
\begin{aligned}
x_{f,evap} > x_i : F_{enth,i}\left(T_i,(\tilde{\rho}h)_i,x_{f,evap},T_{f,evap}\right) &= (x_i - x_{i-1/2})\left[\rho_v c_v\left(T_i - \frac{\Delta x}{2}\frac{dT}{dx}\Big|_{l,i} - T_{pyr}\right)\right] \\
&+(x_{f,evap} - x_i)\left[\rho_v c_v\left(\frac{T_{f,evap}+T_i}{2} - T_{pyr}\right)\right] \\
&+(x_{i+1/2} - x_{f,evap})\left[\rho_v c_v\left(T_{f,evap} + \frac{x_{i+1/2}-x_f}{2}\frac{dT}{dx}\Big|_{r,i} - T_{pyr}\right)\right] \\
&+(x_{i+1/2} - x_{f,evap})\left[\rho_{w,l} c_{w,l}\left(T_{f,evap} + \frac{x_{i+1/2}-x_f}{2}\frac{dT}{dx}\Big|_{r,i} - T_{ref}\right)\right] \\
&-\left(\tilde{\rho}h\right)_i \Delta x_i
\end{aligned}
$$

e. Cell *i* is virgin wet material and does not contain a front:

$$
\begin{aligned}
F_{enth,i}\left(T_i,(\tilde{\rho}h)_i\right) &= \frac{x_i - x_{i-1/2}}{2}\left[\rho_v c_v\left(T_i - \frac{1}{4}\Delta x_i \frac{dT}{dx}\Big|_{l,i} - T_{pyr}\right)\right] \\
&+\frac{x_i - x_{i-1/2}}{2}\left[\rho_{w,l} c_{w,l}\left(T_i - \frac{1}{4}\Delta x_i \frac{dT}{dx}\Big|_{l,i} - T_{ref}\right)\right] \\
&+\frac{x_{i+1/2} - x_i}{2}\left[\rho_v c_v\left(T_i + \frac{1}{4}\Delta x_i \frac{dT}{dx}\Big|_{r,i} - T_{pyr}\right)\right] \\
&+\frac{x_{i+1/2} - x_i}{2}\left[\rho_{w,l} c_{w,l}\left(T_i + \frac{1}{4}\Delta x_i \frac{dT}{dx}\Big|_{r,i} - T_{ref}\right)\right] \\
&-\left(\tilde{\rho}h\right)_i \Delta x_i
\end{aligned}
\qquad (23e)
$$

3.4.2 Constraint 2: motion of the front

For the cells containing a front, we require an extra constraint. To that purpose, we introduce the function $F_f\left(x_f,T_f,T_i\right)$ for cell *i*, containing the pyrolysis front, so that the discretisation of $\left(\rho_v-\rho_c\right)v_{f,pyr}\Delta Q_{pyr} = -k_c\nabla T\big|_c + k_v\nabla T\big|_v$, expression (15), leads to $F_f\left(x_f,T_f,T_i\right)=0$, with the following expression for F_f:

- $$
\begin{aligned}
x_f \le x_i : F_f\left(x_f,T_f,T_i\right) &= \frac{(x_f - x_f^n)}{\Delta t}(\rho_v - \rho_c)\cdot\Delta Q_{pyr}\cdot(x_i - x_f) \\
&+k_c\cdot\frac{T_f - T_{i-1}}{x_f - x_{i-1}}\cdot(x_i - x_f) - k_v(T_i - T_f)
\end{aligned}
\qquad (24a)
$$

- $$
\begin{aligned}
x_f > x_i : F_f\left(x_f,T_f,T_i\right) &= \frac{(x_f - x_f^n)}{\Delta t}(\rho_v - \rho_c)\cdot\Delta Q_{pyr}\cdot(x_f - x_i) \\
&-k_v\frac{T_{i+1} - T_f}{x_{i+1} - x_f}\cdot(x_f - x_i) + k_c(T_f - T_i)
\end{aligned}
\qquad (24b)
$$

For non-charring materials, ρ_c equals zero and the conduction term in the char is replaced by the external heat flux.

Similarly, for the evaporation front, the constraints lead to $F_{f,evap}\left(x_{f,evap}, T_{f,evap}, T_i\right) = 0$, with:

- $$x_{f,evap} \le x_i : F_{f,evap}\left(x_{f,evap}, T_{f,evap}, T_i\right) = \frac{(x_{f,evap} - x^n_{f,evap})}{\Delta t}\rho_{w,l} L_v (x_i - x_{f,evap}) + k_{v,wet} \cdot \frac{T_f - T_{i-1}}{x_{f,evap} - x_{i-1}}(x_i - x_{f,evap}) - k_{v,dry}(T_i - T_{f,evap}) \quad (25a)$$

- $$x_{f,evap} > x_i : F_{f,evap}\left(x_{f,evap}, T_{f,evap}, T_i\right) = \frac{(x_{f,evap} - x^n_{f,evap})}{\Delta t}\rho_{w,l} L_v (x_{f,evap} - x_i) - k_{v,dry}\frac{T_{i+1} - T_{f,evap}}{x_{i+1} - x_{f,evap}}(x_{f,evap} - x_i) + k_{v,wet}(T_{f,evap} - T_i) \quad (25b)$$

We use the notation $k_{v,dry}$ here for clarity. In general, $k = \sum_i \alpha_i k_i$, so that effectively $k_{v,dry} = k_v$ and $k_{v,wet} = \alpha_v k_v + \alpha_{w,l} k_{w,l}$ (see above).

3.4.3 Inversion of the constraints to determine temperature and fronts' position.

Using expressions (23) - (25), for a given enthalpy field, the corresponding temperature field and front positions can be found. However, direct inversion of equations (23)-(25) is a tedious task, since all equations are coupled. Indeed, an expression for a cell *i* does not only involve the local temperature T_i, but also the temperature values of the neighbouring nodes. Since an iterative procedure is adopted anyway, this coupling is not taken into account for the inversion of the system and only the temperature of cell *i* is considered as an unknown in the functions. The neighbouring temperatures are then taken from the previous iteration level (as 'known' quantities). This allows a much cheaper inversion, since every cell can be treated independently.

For cells that do not contain a pyrolysis or evaporation front, the determination of $T_i^{n+1,k+1}$ from $(\tilde{\rho}h)_i^{n+1,k+1}$ is straightforward, setting $F_{enth,i}\left(T_i^{n+1,k+1},(\tilde{\rho}h)_i^{n+1,k+1}\right)=0$, using expressions (23a), (23c) or (23d). E.g. for a cell only containing char material, expression (23a) yields

$$\begin{aligned}F_{enth,i}\left(T_i^{n+1,k+1},(\tilde{\rho}h)_i^{n+1,k+1}\right)=&\frac{x_i-x_{i-1/2}}{2}\left[\rho_c c_c\left(T_i^{n+1,k+1}-\frac{1}{4}\Delta x_i\left.\frac{dT}{dx}\right|_{l,i}^{n+1,k}-T_{pyr}\right)+(\rho_v-\rho_c)\Delta Q_{pyr}\right]\\&+\frac{x_{i+1/2}-x_i}{2}\left[\rho_c c_c\left(T_i^{n+1,k+1}+\frac{1}{4}\Delta x_i\left.\frac{dT}{dx}\right|_{r,i}^{n+1,k}-T_{pyr}\right)+(\rho_v-\rho_c)\Delta Q_{pyr}\right],\\&-(\tilde{\rho}h)_i^{n+1,k+1}\Delta x_i=0\end{aligned}$$

from which $T_i^{n+1,k+1}$ immediately follows.

We focus now on a cell that contains the pyrolysis front. We use the flowchart, discussed above. We consider as first possibility that the update in $\tilde{\rho}h_i$ leads to a variation in the pyrolysis front position, keeping the front temperature constant, equal to T_{pyr}. Then we express:

$$\begin{cases}F_f\left(T_i^{n+1,k+1},x_f^{n+1,k+1};T_{pyr}\right)=0\\F_{enth,i}\left(T_i^{n+1,k+1},x_f^{n+1,k+1};(\tilde{\rho}h)_i^{n+1,k+1},T_{pyr}\right)=0\end{cases}\qquad(26)$$

The notation means that the quantities behind the semi-colon are 'known', whereas the variables ahead of the semi-colon are to be computed. Linearization around $\left(T_i^{n+1,k},x_f^{n+1,k}\right)$ yields a Taylor expansion, with $\Delta T_i=T_i^{n+1,k+1}-T_i^{n+1,k}$ and $\Delta x_f=x_f^{n+1,k+1}-x_f^{n+1,k}$:

$$\begin{aligned}&F_f\left(T_i^{n+1,k},x_f^{n+1,k};T_{pyr}\right)+\frac{F_f\left(T_i^{n+1,k}+\delta T_i,x_f^{n+1,k};T_{pyr}\right)-F_f\left(T_i^{n+1,k},x_f^{n+1,k};T_{pyr}\right)}{\delta T_i}\cdot\Delta T_i\\&\quad+\frac{F_f\left(T_i^{n+1,k},x_f^{n+1,k}+\delta x_f;T_{pyr}\right)-F_f\left(T_i^{n+1,k},x_f^{n+1,k};T_{pyr}\right)}{\delta x_f}\cdot\Delta x_f=0\end{aligned}\qquad(27a)$$

$$\begin{aligned}&F_{enth,i}\left(T_i^{n+1,k},x_f^{n+1,k};(\tilde{\rho}h)_i^{n+1,k+1},T_{pyr}\right)+\frac{F_{enth,i}\left(T_i^{n+1,k}+\delta T_i,x_f^{n+1,k};(\tilde{\rho}h)_i^{n+1,k+1},T_{pyr}\right)-F_{enth,i}\left(T_i^{n+1,k},x_f^{n+1,k};(\tilde{\rho}h)_i^{n+1,k+1},T_{pyr}\right)}{\delta T_i}\cdot\Delta T_i\\&\quad+\frac{F_{enth,i}\left(T_i^{n+1,k},x_f^{n+1,k}+\delta x_f;(\tilde{\rho}h)_i^{n+1,k+1},T_{pyr}\right)-F_{enth,i}\left(T_i^{n+1,k},x_f^{n+1,k};(\tilde{\rho}h)_i^{n+1,k+1},T_{pyr}\right)}{\delta x_f}\cdot\Delta x_f=0\end{aligned}$$

(27b)

For the numerical calculation of the partial derivatives, we use $\delta x_f = 0.001 \cdot \Delta x_i$ and $\delta T_i = 0.1\,\mathrm{K}$.

The equations can be written in the form:

$$\begin{cases} a_{11}\Delta T_i + a_{12}\Delta x_f = b_1 \\ a_{21}\Delta T_i + a_{22}\Delta x_f = b_2 \end{cases}, \tag{28}$$

with $a_{11} = \frac{\delta F_f}{\delta T_i}$; $a_{12} = \frac{\delta F_f}{\delta x_f}$; $b_1 = -F_f\left(T_i^{n+1,k}, x_f^{n+1,k}; T_{pyr}\right)$;

$a_{21} = \frac{\delta F_{enth,i}}{\delta T_i}$; $a_{22} = \frac{\delta F_{enth,i}}{\delta x_f}$; $b_2 = -F_{enth,i}\left(T_i^{n+1,k}, x_f^{n+1,k}; (\tilde{\rho}h)_i^{n+1,k+1}, T_{pyr}\right)$.

This system is solved, using Cramer's method, yielding ΔT_i and Δx_f, and thus $T_i^{n+1,k+1}$ and $x_f^{n+1,k+1}$. The convergence check has been reported above, in section 3.1.

Exactly the same strategy is adopted when the pyrolysis process is not taking place, i.e. $T_f < T_{pyr}$:

$$\begin{aligned} &F_f\left(T_i^{n+1,k+1}, T_f^{n+1,k+1}; x_f^n\right) = 0 \\ &F_{enth,i}\left(T_i^{n+1,k+1}, T_f^{n+1,k+1}; (\tilde{\rho}h)_i^{n+1,k+1}, x_f^n\right) = 0 \end{aligned} \tag{29}$$

Then the perturbations are for T_i and T_f (instead of T_i and x_f) and x_f is assumed to be constant, equal to x_f^n.

3.5 Treatment of the boundaries

In the first cell (when $x_f < x_0$) and the last cell (when $x_f > x_n$), we adopt a piecewise linear extrapolation: T_f is related to x_f such that it is on the straight line through (x_0, T_0) and (x_1, T_1) for the first cell: $F_f\left(x_f, T_f, T_0\right) = T_0 - \frac{T_1^{n+1,k} - T_0}{x_1 - x_0}(x_0 - x_f) - T_f$; for the last cell, we have in a similar manner: $F_f\left(x_f, T_f, T_n\right) = T_n + \frac{T_n - T_{n-1}^{n+1,k}}{x_n - x_{n-1}}(x_f - x_{n-1}) - T_f$. It is clear that we cannot use expressions (24), since these functions return zero by construction of the temperature profile. Hence, the alternative constraint at the boundaries.

The same extrapolation is performed if the evaporation front is in the first or the last cell, yielding constraints: $F_{f,evap}\left(x_{f,evap},T_{f,evap},T_0\right)=T_0-\frac{T_1^{n+1,k}-T_0}{x_1-x_0}(x_0-x_{f,evap})-T_{f,evap}$;

$F_{f,evap}\left(x_{f,evap},T_{f,evap},T_n\right)=T_n+\frac{T_n-T_{n-1}^{n+1,k}}{x_n-x_{n-1}}(x_{f,evap}-x_{n-1})-T_{f,evap}$.

3.6 Discussion: zero-th order temperature field representation

In [25], a zero-th order representation is adopted for the temperature field, i.e. the temperature is uniform in each of the computational cells. The essential difference to the model formulation as presented above is that, when the mushy cell is pyrolysing, its temperature is kept fixed, equal to the pyrolysis temperature. In combination herewith, a computational cell only starts pyrolysing when its temperature becomes equal to the pyrolysis temperature. This has serious consequences on the evolution of the pyrolysis gases mass flow rates and pyrolysis front motion: when the mushy cell has just become pure char, the next cell to pyrolyse must first still heat up to T_{pyr} and during this period, $\dot{m}''_{pyr}$ drops to zero, which is unacceptable. Indeed, as the only heat transfer mechanism towards the virgin material is by conduction, it is inevitable that, at the moment when the formerly pyrolysing cell becomes pure char, the temperature of the neighbouring virgin cell is still below the pyrolysis temperature. This was already recognised in [8], but the problem was not really solved there. A dual mesh technique was introduced, effectively reducing the mentioned undesired phenomenon, but not solving the problem.

4. Discussion of results

We restrict ourselves to configurations where the externally imposed heat flux is not computed from flame radiation, in order to avoid related uncertainty.

As initial condition, there is only virgin material at temperature $T = T_{amb} = 300K$, which is well below the pyrolysis temperature. Unless stated otherwise, all results are obtained with the piecewise linear temperature field representation.

4.1 One-dimensional configuration – charring material

Consider a one-dimensional configuration, with an external radiative heat flux imposed at one side. Accounting for external heat loss from the exposed surface by convection and re-radiation, the net heat flux, entering the solid by conduction, becomes:

$$\dot{q}''_{0-\frac{1}{2}} = \dot{q}''_{cond,0-\frac{1}{2}} = \varepsilon \dot{q}''_{ext} - h\left(T_{surf} - T_{amb}\right) - \varepsilon \cdot \sigma \cdot \left(T_{surf}^4 - T_{amb}^4\right) + \dot{q}''_{conv,0-\frac{1}{2}} \qquad (30)$$

Note that the final term, corresponding to the vapour and volatiles, is negative.

The back surface is perfectly insulated and impervious: $\dot{q}''_{n+\frac{1}{2}} = 0$.

We compare our numerical results to the experiments of [15], which were conducted on a 3.8cm cubic sample of white pine, subjected to a net incident external heat flux of 40kW/m^2 on only one surface. Preconditioning was done on the sample in order to remove the moisture content. The sample was placed on an electronic balance for continuous weight recording, from which the pyrolysis gases mass flow rate could be determined. The temperature was recorded by thermocouples, placed in the sample at three different depths (surface, 5mm and 10mm depth). We also compare our results to the numerical simulations of [5], where an integral model is used. We use the same values for the thermo-physical properties of white pine as in [5]: $\rho_v = 380 kg/m^3$, $c_v = 1196 J/(kg \cdot K)$, $k_v = 0.34 W/(m \cdot K)$, $\rho_c = 76 kg/m^3$, $c_c = 986.8 J/(kg \cdot K)$, $k_c = 0.2 W/(m \cdot K)$ $c_g = 1040 J/(kg \cdot K)$. We also use the same values for emissivity and convection coefficient ($\varepsilon = 0.9, h = 15.0 W/(m^2 K)$) and the same model parameters: ΔQ_{pyr}= *1.2 MJ/kg,* , T_{amb}=*300 K*, T_{pyr}= *658K*. It is evident that the results strongly depend on these values, but a parameter study is not the topic of the present paper. Our basic configuration consists of 40 cells and a physical time step equal to 0.5s. We discuss the dependence of the results on these choices below.

In Figure 5, we present the evolution of the pyrolysis gases mass flow rate as function of time. A first important observation is that we reproduce the numerical results of [5]. Per se, this is not surprising as we use identical settings for the configuration and material properties, but the methodology is strongly different. Here, we use a simple technique with a fixed computational mesh that is extendable to multi-dimensional configurations (see below), whereas integral type models are intrinsically one-dimensional. Agreement with the experimental data is not perfect. In the experiments, pyrolysis starts immediately. In the numerical simulations, the material first needs to heat up (at the exposed surface) up to the pyrolysis temperature before the pyrolysis process can start and pyrolysis gases are generated. As mentioned in [5], the peak mass flow rate corresponds very well to the experimentally reported value. Agreement with the experimental data can be improved by variation of the material properties or by inclusion of finite rate kinetics.

The observations for the temperature evolution inside the material, as measured by thermocouples at the surface and at depths equal to 5mm and 10mm, are very similar. We agree with the statement in [5] that the relatively poor agreement at the deepest location is due to the simplicity of the pyrolysis model. The temperature rises more rapidly than in the experiments. Adjustment of material properties could lead to better agreement with experimental observations.

We now discuss the dependence of the results on the number of computational cells and the physical time step (Figure 6). Clearly, differences are very small, even for a number as low as 20 cells. Table 1 quantifies this, reporting the maximum mass flow rate value and the relative error, compared to the results obtained for a 320 cells mesh. We determine $\dot{m}''_{pyr,\max}$ by constructing a parabola through the obtained discrete maximum value and the values obtained at the previous and subsequent time step. The relative error is computed as

$\left\| \dot{m}''_{pyr,\max} - \dot{m}''_{pyr,\max,320} \right\| / \left\| \dot{m}''_{pyr,\max,320} \right\|$ .The errors remain well below 5%, even for the coarsest mesh. This is typically less than other uncertainties and implies that the model and method are robust with respect to the number of computational mesh cells.

We also show the effect of the physical time step size on the results, for the configuration with 40 cells. Except for the two largest time steps, deviations between the curves are again very small (see Table 2). Now the result with $\Delta t = 0.1s$ is used as reference value to compute the relative errors. Again, the error remains well below 5%, unless time steps as large as 10s are taken. From table 2 it is thus clear that quite large time steps can be taken with the present model and method, without substantial loss in accuracy. In combination with the robustness with respect to the number of computational cells, this property makes the present model and method appealing for coupling to CFD simulations, in particular in multi-dimensional configurations (as conduction in the solid material is readily taken into account, see below).

So far, we focused on results, obtained with a piecewise linear temperature field representation. Figure 7 (left) reveals that this is essential to obtain a continuous mass flow rate evolution in time. Indeed, a zero-th order temperature field representation, i.e. a uniform temperature per computational cell, as might be the first natural choice, is not sufficient: the pyrolysis gases mass flow rate evolution in time reveals discontinuities. As explained above, the mass flow rate (21) inevitably always drops to zero when the char fraction in the mushy cell becomes equal to 1. Clearly, this behaviour is not physical. Moreover, it makes coupling to CFD gas phase combustion simulations impossible: depending on the chemistry model applied, this may extinguish the flame (while this might not be the case in reality). Also, it is not easy to reconstruct (or 'guess') the actual pyrolysis gases mass flow rate evolution in time from the results, obtained with the zero-th order temperature field representation. The only constraint for reconstruction that can readily be imposed, is that the total mass consumed, after char fraction evolution from 0 to 1, must be the same in both cases, but this

constraint does not tell anything about the rates of mass loss. It is thus impossible to reconstruct the dashed line from the solid line results in fig. 7. This is particularly true during the simulations (when the future is un-known), but even the application of a filter afterwards will not result in the dashed line.

Figure 7 (right) shows the evolution of the surface temperature as function of time. For this quantity, there is no derivation with respect to time and the curves are closer together. A more or less stepwise evolution is observed with the zero-th order representation, though. Indeed, as the pyrolysis mass flow rate drops to zero, there are instantaneously no convective heat losses with the pyrolysis gases and the material heats up more rapidly than when there is a continuous flow of pyrolysis gases.

Figure 8 shows the effect of moisture. We consider the same configuration, but add 5, 10 and 15% unbound moisture. The latent heat of vaporisation is $L_v = 2.27 \cdot 10^6 \, {}^{J}\!/_{kg}$ and the thermal capacities of liquid water and water vapour are $c_{w,l} = 4184 \, {}^{J}\!/_{(kgK)}$ and $c_{w,v} = 2000 \, {}^{J}\!/_{(kgK)}$. In figure 8, the total mass loss rate is the sum of the water vapour mass flow rate and the pyrolysis gases mass loss rate. An increase in the moisture content in the solid clearly leads to an increase in the duration of the pyrolysis process. Indeed, part of the incoming heat flux is consumed in the evaporation process of the unbound moisture. Focusing on the first 100s (figure 8, right) shows the onset of the evaporation and pyrolysis processes. Obviously, the evaporation process starts already when the surface temperature equals 373K, while the pyrolysis process only starts when it equals T_{pyr}. A sudden drop in the total mass flow rate is observed when the evaporation front reaches the back surface, because the evaporation front reaches this surface with a non-zero velocity. The pyrolysis gases mass flow rate increases then, because no heat is consumed in the evaporation process any more. The remainder of the pyrolysis process takes place in dry virgin material, so that very similar mass flow rate profiles are observed. To a good approximation, the initial moisture bulk density determines

the shift of the profiles. The higher the moisture content, the more the curves are shifted to the right (longer global evaporation/pyrolysis process).

Figure 9 shows the temperature distribution in the solid at the different depths (surface, 5mm and 10mm). With the increase in moisture content in the solid, the inner solid temperature rises more slowly. Agreement with the experimental data is not perfect (in particular at 5mm depth), but the global trends are well captured.

4.2 One-dimensional configuration – Non-charring material

We now discuss (dry) PMMA, as an example of non-charring material. We apply the same pyrolysis model as in section 4.1, setting ρ_c, the convection by pyrolysis gases and the conduction fluxes in the char to zero. The front surface of the virgin material, which is now also the pyrolysis front, is exposed to the external heat flux. We use the thermo-physical properties from [21] and [26]: ρ_v=1150kg/m^3, c_v=1.42·10^{3}J/(kgK), ΔQ_{pyr}=1.007·10^{6}J/kg, k_v=1.85·10^{-1}W/(mK). The PMMA solid is 3cm thick. The pyrolysis temperature is set to T_{pyr}=630K [26]. We use 80 cells and a time step of 0.5s. The back surface is perfectly insulated and the boundary condition at the front surface reads [21]:

$$x = x_f ; \quad \dot{q}''_{net} = 46 - h\left(T_s - T_{amb}\right) - \varepsilon\sigma T_s^4 \qquad (kW/m^2) .$$

Figure 10 shows the mass loss rate evolution in time. In the results 'with losses', we use h = 20W/(m^{2}K) and ε = 0.92. In the results 'without losses', $h = \varepsilon = 0$. Agreement with the data of [21] is very good when the heat losses are accounted for. Obviously, when the convection and radiation losses are not taken into account, the mass loss rate is higher and the material is consumed in a shorter time period.

The mass loss begins when the surface temperature reaches T_{pyr}. After some time, the mass loss rate attains a quasi-steady state: the incoming heat flux provides energy for the pyrolysis process and for heat conduction into the virgin solid. After a while, the mass loss rate rises, due to the back effect: less heat is conducted into the remainder of the solid material and thus

a larger part of the external heat flux is utilized for the pyrolysis process. Obviously, this is more pronounced when there is no heat loss at the exposed surface. All these issues are well captured with the present model.

4.3 Multi-dimensional configuration – Upward flame spread

We now illustrate that the model is in principle able to cope with multi-dimensional configurations by means of a numerical test case of upward flame spread. Extensions to more dimensions can be done with different degrees of complexity. Here, we work with a 'pseudo-2D' (or 'pseudo-3D') model: conduction inside the solid material is allowed in all directions, but the pyrolysis front in each row (or column) of computational cells is parallel to the solid material surface, exposed to the external heat flux, and moves perpendicular to that surface. The pyrolysis gases also flow out of the material, perpendicular to the exposed surface. These assumptions are mostly valid when the material thickness is much smaller than the other dimensions, as is mostly the case for fire (or flame spread) configurations. We consider dry material, but extension to wet material is straightforward.

As a test, consider a vertically oriented sample with the same material properties as described in section 4.1. The sample is 10cm high and we consider three thicknesses: 3mm, 5mm and 1cm. We use square cells of 0.5mm x 0.5mm. The physical time step size is set to 0.1s. The back, top and bottom surfaces are perfectly insulated. We impose an external heat flux of 40kW/m^2 in a region of 5mm at the bottom of the front surface. By conduction, the material starts to heat up.

As soon as pyrolysis starts, we use a correlation for upward flame spread [27] to calculate the flame height $y_f(t)$ from the pyrolysis height $y_p(t)$ (i.e. the height over which the material has pyrolysed at its front surface or, alternatively, where the front surface temperature exceeds T_{pyr}): $y_f(t) = y_p(t) + 0.0433\left(\dot{Q}_b' + \dot{Q}_m'\right)^{2/3}$. In our case, the igniter heat flux $\dot{Q}_b'$ equals 40kW/m^2 x 0.005m = 0.2kW/m. The heat release rate from pyrolysis is computed every time

step as $\dot{Q}_f^{'} = \Delta H_c \int_0^{y_p} \dot{m}_{pyr}^{''} dy$, using $\Delta H_c = 16 MJ/kg$. A constant value of 25kW/m^2 is added to the external heat flux in the region $y < y_f(t)$, resembling radiative heat feedback from flames. Convective and radiative heat losses from the front surface are also considered as in section 4.1, with $\varepsilon = 0.9, h = 15.0 W/\left(m^2 K\right)$.

Figure 11 shows the temperature and char fraction fields evolution in time for a material thickness of 5mm. The multi-dimensionality in the fields is clearly observed. Obviously, the material heats up at the bottom (from the left surface) first. Pyrolysis also starts there. After the onset of pyrolysis, there is an acceleration in heating up and pyrolysis, because the flames rapidly cover a large part of the material.

Figure 12 provides a more quantitative illustration. In the left column, the pyrolysis gases mass flow rates evolutions in time are shown at different heights, for the different material thicknesses. One-dimensional configuration results are also shown, for comparison purposes, as explained below.

At height y = 0mm (i.e. the bottom of the material), a heat flux of 25kW/m^2 is added at the front surface as soon as pyrolysis starts, as mentioned above. The situation is almost one-dimensional. This is reflected in the very small differences with the first 1D result (for which the set-up is as in section 4.1, adding 25kW/m^2 at the front surface as soon as pyrolysis starts). As there are some conductive heat losses in the upward direction, the pyrolysis front motion is somewhat slower and the mass flow rates are somewhat lower than in the one-dimensional configuration. This is true for all thicknesses. The thicker the material, the longer it takes for pyrolysis to start and the longer the pyrolysis process lasts.

At height y = 5cm and y = 9cm, the situation is also practically one-dimensional. Obviously, the higher in the material, the longer it takes for pyrolysis to start, as radiative heat from the flames is required. Except for a shift in time, the results are very similar to the 1D results,

with a constant external heat flux of 25kW/m^2 imposed at the front surface. The temperature evolution in time (figure 13, right) reveals that there is practically no pre-heating by conduction by the time pyrolysis starts. Thus, the simulation results confirm that radiative heat transfer from the flames is predominant. During the pyrolysis process, the net effect of conductive heat fluxes in the upward direction is very small.

At height y = 1cm, on the other hand, the situation is more complex. Here, there is pre-heating by conduction (see figure 13, right) before the onset of pyrolysis in the material. Also, there is a second, high, peak in the mass flow rate, again due to incoming conductive heat flux from below. [Note that we do not remove the igniter when the pyrolysis starts. This also explains the higher equilibrium temperatures at y = 0mm (and y = 1cm), compared to the values at higher locations (figure 13).]

In figure 12, we also show the evolution in time of the pyrolysed zone at the front surface (y_p) and the height of the flame tip (y_f). Clearly, at the onset of pyrolysis, according to the applied correlation, the flames immediately cover a substantial part of the material. The flames are higher for the thinner material, as the pyrolysis gases mass flow rates are higher. The radiative feedback from the flames heats up the material. Consequently, there is accelerating flame spread, due to the positive feedback loop. Obviously, there is a delay in the evolution of y_p, compared to y_f. When the flames cover the entire front surface (y_f = 0.1m, see right column of figure 12), there is an evolution towards a more or less steady regime, with an almost linear increase of y_p. This is explained by the relatively constant incoming heat flux and outgoing total pyrolysis mass flow rates. As y_p approaches the top surface, an acceleration is observed again, as there are no conductive heat losses at the top surface and thus, due to net incoming conductive heat fluxes from below, the pyrolysis front moves more rapidly than in a one-dimensional configuration. Note that y_f reaches a maximum value when y_p has reached the top surface and the total pyrolysis mass flow rate reaches its maximum

value. As the material burns out, the flames become shorter and in fact disappear in the end. This is not seen here, because the igniter flux is kept in the correlation of [27], as mentioned above. We also assume that the flames have their origin at y = 0mm at all times, even if the material is pure char after a while. This can easily be modified, but this is not relevant for the present paper.

Figure 13, showing front surface temperature evolutions in time, supports these findings. At heights where the situation resembles a one-dimensional configuration, we observe three stages: heat-up phase before pyrolysis; pyrolysis; heat-up phase of char (up to the equilibrium end temperature). These stages are readily distinguished by sudden variations in the temperature evolution. At y = 1cm, though, we see the effect of conduction again: there is pre-heating before any flames are seen and in the end, there is no sudden variation in the temperature evolution. Instead, there is a smooth transition to the equilibrium end temperature. Note that the equilibrium end temperature at y = 5cm and y = 9cm almost exactly matches the equilibrium end temperature: the configuration is practically one-dimensional, with negligible net effect of conductive fluxes in the upward direction. At y = 0mm, there are net conductive losses in the upward direction, so that the equilibrium end temperature is somewhat lower than in the purely one-dimensional configuration.

Obviously, the temperature rise occurs later for higher positions in the material.

To conclude this discussion, we draw the attention to the temperature evolution at y = 5cm for the 1cm thick material. Before pyrolysis takes place at that height, there is a sudden decrease in the temperature evolution (between t = 40s and 80s). This is due to the drop in y_f around y = 5cm in this period (see figure 12): when y_f drops below this height, there is no heat-up any more and, due to the convective and radiative heat losses from the front surface, the net effect is ‘cooling down’, leading to a decrease in temperature. This phenomenon is not observed for the smaller material thicknesses, as the pyrolysis mass flow rates are higher.

It is appealing that the present, simplified model, captures all the mentioned features automatically.

5. Summary and conclusions

Starting from a basic thermodynamic description of pyrolysis phenomena, a simplified pyrolysis model was described in detail. The basic model quantity is enthalpy, computed from the specific enthalpies of five constituents (dry virgin material, char, pyrolysis gases, liquid water and water vapour). The concept of heat of pyrolysis and its relation to formation enthalpies of individual constituents was revisited. It was explained how the developed model takes advantage of the use of pyrolysis heat to avoid the need for knowledge of the formation enthalpies of all individual constituents.

The major assumption is that pyrolysis and evaporation are isothermal processes, taking place at infinitely thin fronts. The motion of each front is computed by means of a local mass and energy balance.

All equations are solved on a fixed computational mesh, which makes the model appealing for general spread simulations. Indeed, it is easy to implement and applicable in three dimensions, for thermally thick or thin charring and non-charring materials, possibly containing moisture initially. The model can be combined with transport models for water liquid/vapour and pyrolysis gases in the solid material. A char oxidation model can also be incorporated.

The numerical implementation and solution procedure have also been described. The model has then been applied to dry and wet charring materials, to non-charring materials and to a multi-dimensional configuration, resembling upward flame spread.

Good agreement was illustrated for mass flow rates of pyrolysis gases in dry charring and non-charring materials (to which the model is directly applicable). The model formulation is robust with respect to several numerical aspects: the dependence of the results on the

computational mesh cells' size and the physical time step size is small. Yet, in order to obtain continuous and smooth variations in time, it is essential to adopt a piecewise linear representation of the temperature field. With a constant temperature per computational cell, as is usually done, discontinuous evolutions of pyrolysis gases mass flow rates are obtained, regardless of the physical time step and mesh size.

The effect of moisture is well captured: the pyrolysis process becomes slower as heat is consumed during the vaporisation process.

Finally, we illustrated that the model can deal with multi-dimensional configurations by means of a test case, resembling upward flame spread. Many physical phenomena were explained and automatically captured by the present, simplified model.

6. Acknowledgements

This research is funded by project G.0130.06 of the Fund of Scientific research – Flanders (Belgium) (FWO-Vlaanderen). The fourth author is Postdoctoral Fellow of the Fund of Scientific research – Flanders (Belgium) (FWO-Vlaanderen).

7. References

1. C. di Blasi, *Combust. Flame* 97: 225-239 (1994).
2. B. Moghtaderi, V. Novozhilov, D. Fletcher and J. H. Kent, *Fire Mat.* 21: 7-16 (1997).
3. F. Jia, E. R. Galea, M. K. Patel, *Fire Mat.* 23: 71-78 (1999).
4. M. J. Spearpoint and J. G. Quintiere, *Combust. Flame* 123: 308-325 (2000).
5. W. G. Weng and W. C. Fan, *Fire Mat.* 31: 463-475 (2007).
6. E. Theuns, B. Merci, J. Vierendeels and P. Vandevelde, *Fire Mat.* 29: 463-475 (2005).
7. E. Theuns, J. Vierendeels and P. Vandevelde, *J. Comp. Appl. Math.* 168: 471-479 (2003).
8. Z. Yan and G. Holmstedt, *Fire Saf. J.* 27: 201-238 (1996).
9. C. di Blasi, *Prog. Energy Combust. Sci.* 19: 71-104 (1993).

10. Y. Chen, M. A. Delichatsios and V. Motevalli, *Combust. Sci.Techn.* 88: 309-328 (1993).
11. R. E Lyon, *Fire Mat*. 24: 179-186 (2000).
12. J. G Quintere, A Semi-Quantitative Model for the Burning Rate of Solid Materials, NISTIR 4840, 1992.
13. J. G Quintere and N Iqbal, *Fire Mat*. 18: 89-98 (1994).
14. A. Tewarson and S. D Ogden, *Combust. Flame* 89: 237-259 (1992).
15. T. Kashiwagi, T. J. Ohlemiller and K. Werner, *Combust. Flame*, 69,: 331-345, (1987).
16. H.C. Kung, *Combust. Flame* 18: 185-195 (1972).
17. B. Fredlund, A Model for Heat and Mass Transfer in Timber Structures During Fire, PhD Thesis, Lund (1988).
18. B. Fredlund, *Fire Saf. J*. 20: 39-69 (1993).
19. A. Atreya, Pyrolysis, Ignition and Fire Spread on Horizontal Surfaces of Wood, Harward University, Div. of Applied Science, Cambridge. March 1984.
20. M. Sibulkin, *IAFSS - Proc. First Int. Symp.* 391-400 (1986).
21. D. Drysdale, *An Introduction to Fire Dynamics,* Wiley Publications, 1998.
22. E. Mikkola, *IAFSS - Proc. Third Int. Symp.* 547-556 (1991).
23. M.W. Dechatsios, P. Wu, M.A. Delichatsios, et al. , *IAFSS - Proc. Fourth Int. Symp.* 421-432 (1994).
24. N. Boonmee, Theoretical and Experimental Study of Autoignition of Wood, PhD Thesis, University of Maryland (2004).
25. E. Theuns E, *Numerical modelling of flame spread.* PhD Thesis, Ghent University-UGent, Faculty of Engineering (2003).
26. Y. Sohn, S.W. Baek and T. Kashiwagi, *Combust. Sci. and Techn.* 145: 83-108 (1999).
27. E. G. Brehob, C. I. Kim, A. K. Kulkarni, *Fire Safety Journal* 36: 225-240 (2001).

APPENDIX A. Model Description in terms of Partial Differential Equations (PDE)

A1. Mass Equations for the Constituents

For the sake of clarity in the next section, we first describe the mass equations for each of the five constituents. The five equations read (for a one-dimensional configuration):

$$\begin{cases} \dfrac{\partial \tilde{\rho}_v}{\partial t} = -\dot{\omega}_g(x)\dfrac{\rho_v}{\rho_v - \rho_c} \\ \dfrac{\partial \tilde{\rho}_c}{\partial t} = \dot{\omega}_g(x)\dfrac{\rho_v}{\rho_v - \rho_c} \\ \dfrac{\partial \tilde{\rho}_g}{\partial t} + \dfrac{\partial \tilde{\rho}_g u_g}{\partial x} = \dot{\omega}_g(x) \\ \dfrac{\partial \tilde{\rho}_{w,l}}{\partial t} = -\dot{\omega}_{w,v}(x) \\ \dfrac{\partial \tilde{\rho}_{w,v}}{\partial t} + \dfrac{\partial \tilde{\rho}_{w,v} u_{w,v}}{\partial x} = \dot{\omega}_{w,v}(x) \end{cases} \tag{A.1}$$

Processes only take place at the pyrolysis front ($x_{f,pyr}$) and the evaporation front ($x_{f,evap}$), so that the RHS in (A.1) is zero in all equations elsewhere (see next section).

Note that virgin material, char and water as a liquid do not move in our model formulation, so that their velocities are zero. We also recall that the notation refers to local densities. For char, e.g., the local density can only take 2 values:

$$\begin{aligned} &\tilde{\rho}_c = \rho_c \text{ if } x < x_{f,pyr} \\ &\tilde{\rho}_c = 0 \text{ if } x > x_{f,pyr} \end{aligned} \tag{A.2}$$

The convective velocities u_g and $u_{w,v}$ stem from a transport model. In our model, their value equals infinity, i.e. pyrolysis gases and water vapour immediately leave the solid matrix, as soon as they are created. However, the products … remain finite.

The production rates of gases and water vapour are related to the speed of the front motion, as is discussed next.

A.2. Motion of Pyrolysis Front and Evaporation Front

The motion of the pyrolysis front is determined from a local mass balance equation:

$$\dot{\omega}_g = \left(\rho_c - \rho_v\right)\frac{dx_{f,pyr}}{dt}\delta\left(x - x_{f,pyr}\right) \tag{A.3}$$

where $\delta(\ )$ is the Dirac-functional, defined as:

$$\begin{cases} \delta\left(x-a\right) = \begin{cases} 0 \text{ if } x \neq a \\ \infty \text{ if } x = a \end{cases} \\ \int_{-\infty}^{+\infty} \delta\left(x-a\right) = 1 \end{cases} \tag{A.4}$$

Indeed: integrating expression (A.3) over a control volume around the pyrolysis front yields:

$$\int_{CV} \dot{\omega}_g dV = \int_{CV} \left(\rho_c - \rho_v\right)\frac{dx_{f,pyr}}{dt}\delta\left(x - x_{f,pyr}\right)dV = \left(\rho_c - \rho_v\right)\frac{dx_{f,pyr}}{dt} S \underbrace{\int \delta\left(x - x_{f,pyr}\right)dx}_{1} \tag{A.5}$$

which exactly corresponds to a mass balance over the pyrolysis front (cf. eq. 16).

A similar expression can be derived for the motion of the evaporation front:

$$\dot{\omega}_{w,v} = \rho_{w,l}\frac{dx_{f,evap}}{dt}\delta\left(x - x_{f,evap}\right) \tag{A.6}$$

A.3. Enthalpy Equation

The enthalpy equation reads:

$$\frac{\partial \tilde{\rho} h}{\partial t} + \frac{\partial \tilde{\rho} h u}{\partial x} = -\frac{\partial}{\partial x} q_{cond} \tag{A.7}$$

Using (1) and (13), (A.7) becomes:

$$\sum_{\alpha}\frac{\partial \tilde{\rho}_\alpha h_\alpha}{\partial t} + \sum_{\alpha}\frac{\partial \tilde{\rho}_\alpha h_\alpha u_\alpha}{\partial x} = -\frac{\partial}{\partial x}\left(k\frac{\partial T}{\partial x}\right) \tag{A.8}$$

In the convection term, the velocity of the constituent must be taken. Thus, the convection term only appears for gas and water vapour in our model.

Further elaboration yields:

$$\underbrace{\sum_{\alpha}\tilde{\rho}_\alpha\left[\frac{\partial h_\alpha}{\partial t} + u_\alpha\frac{\partial h_\alpha}{\partial x}\right]}_{I} + \underbrace{\sum_{\alpha} h_\alpha\left[\frac{\partial \tilde{\rho}_\alpha}{\partial t} + \frac{\partial \tilde{\rho}_\alpha u_\alpha}{\partial x}\right]}_{II} = -\frac{\partial}{\partial x}\left(k\frac{\partial T}{\partial x}\right) \tag{A.9}$$

We will now discuss each of the 2 terms in the LHS. Using (2), the dependency on formation enthalpies disappears:

$$\sum_{\alpha} \tilde{\rho}_{\alpha} \left[\frac{\partial}{\partial t} \int_{T_{ref}}^{T} c_{\alpha}(T)\, dT + u_{\alpha} \frac{\partial}{\partial x} \int_{T_{ref}}^{T} c_{\alpha}(T)\, dT \right], \tag{A.10}$$

For term II, expressions (A.1) yield:

$$\begin{aligned} &\dot{\omega}_g(x) h_g(T) + \frac{\rho_c}{\rho_c - \rho_v} \dot{\omega}_g(x) h_c(T) - \frac{\rho_c}{\rho_c - \rho_v} \dot{\omega}_g(x) h_v(T) \\ &+ \dot{\omega}_{w,v}(x) h_{w,v}(T) - \dot{\omega}_{w,v}(x) h_{w,l}(T) \end{aligned} \tag{A.11}$$

Term II only differs from zero at the two fronts, which are at pyrolysis or evaporation temperature:

$$\begin{aligned} &\dot{\omega}_g(x) \left[h_g(T_{pyr}) + \frac{\rho_c}{\rho_c - \rho_v} h_c(T_{pyr}) - \frac{\rho_c}{\rho_c - \rho_v} h_v(T_{pyr}) \right] \\ &+ \dot{\omega}_{w,v}(x) \left[h_{w,v}(T_{evap}) - h_{w,l}(T_{evap}) \right] \end{aligned} \tag{A.12}$$

or, with (4) and (8):

$$\dot{\omega}_g(x) \Delta Q_{pyr} + \dot{\omega}_{w,v}(x) L_v \tag{A.13}$$

As such, the enthalpy equation (A.9) reads:

$$\begin{aligned} &\tilde{\rho}_v \frac{\partial}{\partial t} \int_{T_{ref}}^{T} c_v(T)\, dT + \tilde{\rho}_c \frac{\partial}{\partial t} \int_{T_{ref}}^{T} c_c(T)\, dT + \tilde{\rho}_g \frac{\partial}{\partial t} \int_{T_{ref}}^{T} c_g(T)\, dT \\ &+ \tilde{\rho}_{w,l} \frac{\partial}{\partial t} \int_{T_{ref}}^{T} c_{w,l}(T)\, dT + \tilde{\rho}_{w,v} \frac{\partial}{\partial t} \int_{T_{ref}}^{T} c_{w,v}(T)\, dT \\ &+ \tilde{\rho}_g u_g \frac{\partial}{\partial x} \int_{T_{ref}}^{T} c_g(T)\, dT + \tilde{\rho}_{w,v} u_{w,v} \frac{\partial}{\partial x} \int_{T_{ref}}^{T} c_{w,v}(T)\, dT \\ &+ \dot{\omega}_g(x) \Delta Q_{pyr} + \dot{\omega}_{w,v}(x) L_v = \frac{\partial}{\partial x} \left(k \frac{\partial T}{\partial x} \right) \end{aligned} \tag{A.14}$$

The enthalpy equation can be simplified at positions where no front is present. In that case, the heat input by conduction and convection is used only to modify the temperature:

$$\begin{aligned}
&\tilde{\rho}_v \frac{\partial}{\partial t}\int_{T_{ref}}^{T} c_v(T)dT + \tilde{\rho}_c \frac{\partial}{\partial t}\int_{T_{ref}}^{T} c_c(T)dT + \tilde{\rho}_g \frac{\partial}{\partial t}\int_{T_{ref}}^{T} c_g(T)dT \\
&+\tilde{\rho}_{w,l} \frac{\partial}{\partial t}\int_{T_{ref}}^{T} c_{w,l}(T)dT + \tilde{\rho}_{w,v} \frac{\partial}{\partial t}\int_{T_{ref}}^{T} c_{w,v}(T)dT \\
&= \frac{\partial}{\partial x}\left(k\frac{\partial T}{\partial x}\right) - \left[\tilde{\rho}_g u_g \frac{\partial}{\partial x}\int_{T_{ref}}^{T} c_g(T)dT + \tilde{\rho}_{w,v} u_{w,v} \frac{\partial}{\partial x}\int_{T_{ref}}^{T} c_{w,v}(T)dT\right]
\end{aligned} \tag{A.15}$$

At the front positions, during evaporation or pyrolysis, the heat front motion is governed by the heat balance. Consider e.g. the evaporation front. Introducing the notation $h_{s,i} = \int_{T_{ref}}^{T} c_i dT$ for the sensible enthalpy of a constituent, and … equation (A.14) becomes:

$$\begin{aligned}
&\tilde{\rho}_v \frac{\partial h_{s,v}}{\partial t} + \tilde{\rho}_c \frac{\partial h_{s,c}}{\partial t} + \tilde{\rho}_g \frac{\partial h_{s,g}}{\partial t} + \tilde{\rho}_g u_g \frac{\partial h_{s,g}}{\partial x} \\
&+\tilde{\rho}_{w,l} \frac{\partial h_{s,w,l}}{\partial t} + \tilde{\rho}_{w,v} \frac{\partial h_{s,w,v}}{\partial t} + \tilde{\rho}_{w,v} u_{w,v} \frac{\partial h_{s,w,v}}{\partial x} \\
&+\rho_{w,l} \dot{x}_{f,evap} \delta\left(x - x_{f,evap}\right) L_v = \frac{\partial}{\partial x}\left(k\frac{\partial T}{\partial x}\right)
\end{aligned} \tag{A.16}$$

According to our model, the temperature remains 373K. So, for an observer moving with the evaporation front, $\frac{Dh_s}{Dt} = \frac{dh_s}{dT}\frac{DT}{dt} = 0$ for each of the constituents, with $\frac{D}{Dt}$:

$$\frac{D\bullet}{Dt} = \frac{\partial \bullet}{\partial t} + \dot{x}_{f,evap} \frac{\partial \bullet}{\partial x} \tag{A.17}$$

Introducing this in equation (A.16), yields:

$$\begin{aligned}
&-\tilde{\rho}_v \dot{x}_{f,evap} \frac{\partial h_{s,v}}{\partial x} - \tilde{\rho}_c \dot{x}_{f,evap} \frac{\partial h_{s,c}}{\partial x} + \tilde{\rho}_g \left(u_g - \dot{x}_{f,evap}\right) \frac{\partial h_{s,g}}{\partial x} \\
&-\tilde{\rho}_{w,l} \dot{x}_{f,evap} \frac{\partial h_{s,w,l}}{\partial x} + \tilde{\rho}_{w,v} \left(u_{w,v} - \dot{x}_{f,evap}\right) \frac{\partial h_{s,w,v}}{\partial x} \\
&+\rho_{w,l} \dot{x}_{f,evap} \delta\left(x - x_{f,evap}\right) L_v = \frac{\partial}{\partial x}\left(k\frac{\partial T}{\partial x}\right)
\end{aligned} \tag{A.18}$$

At the front, $x = x_{f,evap}$, temperature is a continuous function and its derivative is piecewise continuous, with a step at the front position. The local densities of water as a liquid and as a

vapour are also piecewise continuous, with a step at the front. Thus, the sum of the first five terms is a step function at the evaporation front and the leading term is the sixth term:

$$LHS = \rho_{w,l}\dot{x}_{f,evap}\delta\left(x - x_{f,evap}\right)L_v + O\left(H\left(x - x_{f,evap}\right)\right) + O\left(continuous\right) \tag{A.19}$$

The notation *H(x-a)* refers to the Heaviside function: *H(x-a) = 0 for x < a; H(x-a) = 1 for x ≥ a.*

For the temperature derivative at the front (in the HRS), we use indices *l* for the left front value limit and *r* for the right front value limit:

$$k\frac{\partial T}{\partial x} = \left(k\frac{\partial T}{\partial x}\right)_l + H\left(x - x_{f,evap}\right)\left[\left(k\frac{\partial T}{\partial x}\right)_r - \left(k\frac{\partial T}{\partial x}\right)_l\right] \tag{A.20}$$

so that:

$$\begin{aligned} RHS = \frac{\partial}{\partial x}\left(k\frac{\partial T}{\partial x}\right) &= \frac{\partial}{\partial x}\left(k\frac{\partial T}{\partial x}\right)_l + H\left(x - x_{f,evap}\right)\frac{\partial}{\partial x}\left[\left(k\frac{\partial T}{\partial x}\right)_r - \left(k\frac{\partial T}{\partial x}\right)_l\right] \\ &+ \left[\left(k\frac{\partial T}{\partial x}\right)_r - \left(k\frac{\partial T}{\partial x}\right)_l\right]\delta\left(x - x_{f,evap}\right) \\ &= \left[\left(k\frac{\partial T}{\partial x}\right)_r - \left(k\frac{\partial T}{\partial x}\right)_l\right]\delta\left(x - x_{f,evap}\right) + O\left(H\left(x - x_{f,evap}\right)\right) + O\left(continuous\right) \end{aligned} \tag{A.21}$$

Thus, to leading order, equation (A.18) becomes:

$$\rho_{w,l}\dot{x}_{f,evap}L_v = \left(k\frac{\partial T}{\partial x}\right)_r - \left(k\frac{\partial T}{\partial x}\right)_l \tag{A.22}$$

For the pyrolysis front, a similar expression can be derived:

$$\left(\rho_c - \rho_v\right)\dot{x}_{f,pyr}\Delta Q_{pyr} = \left(k\frac{\partial T}{\partial x}\right)_r - \left(k\frac{\partial T}{\partial x}\right)_l \tag{A.23}$$

Equations (A.22) and (A.23) were derived from the finite volume formulation in the paper, yielding the same expressions (15) and (17).

Figures

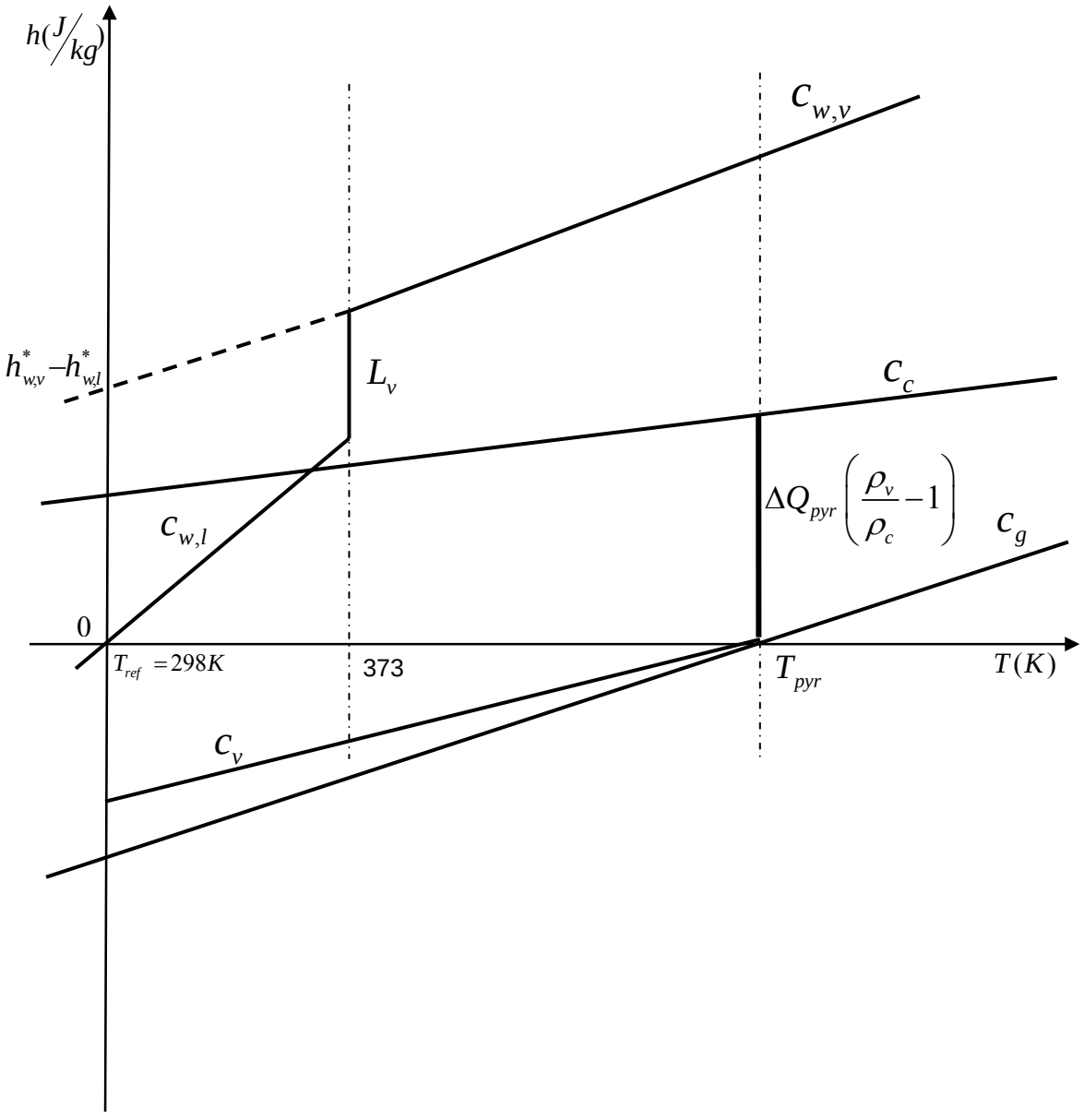
$h(J/kg)$
$c_{w,v}$
$h^*_{w,v} - h^*_{w,l}$
L_v
c_c
$\Delta Q_{pyr}\left(\frac{\rho_v}{\rho_c} - 1\right)$
$c_{w,l}$
c_g
0
$T_{ref} = 298K$
373
T_{pyr}
$T(K)$
c_v

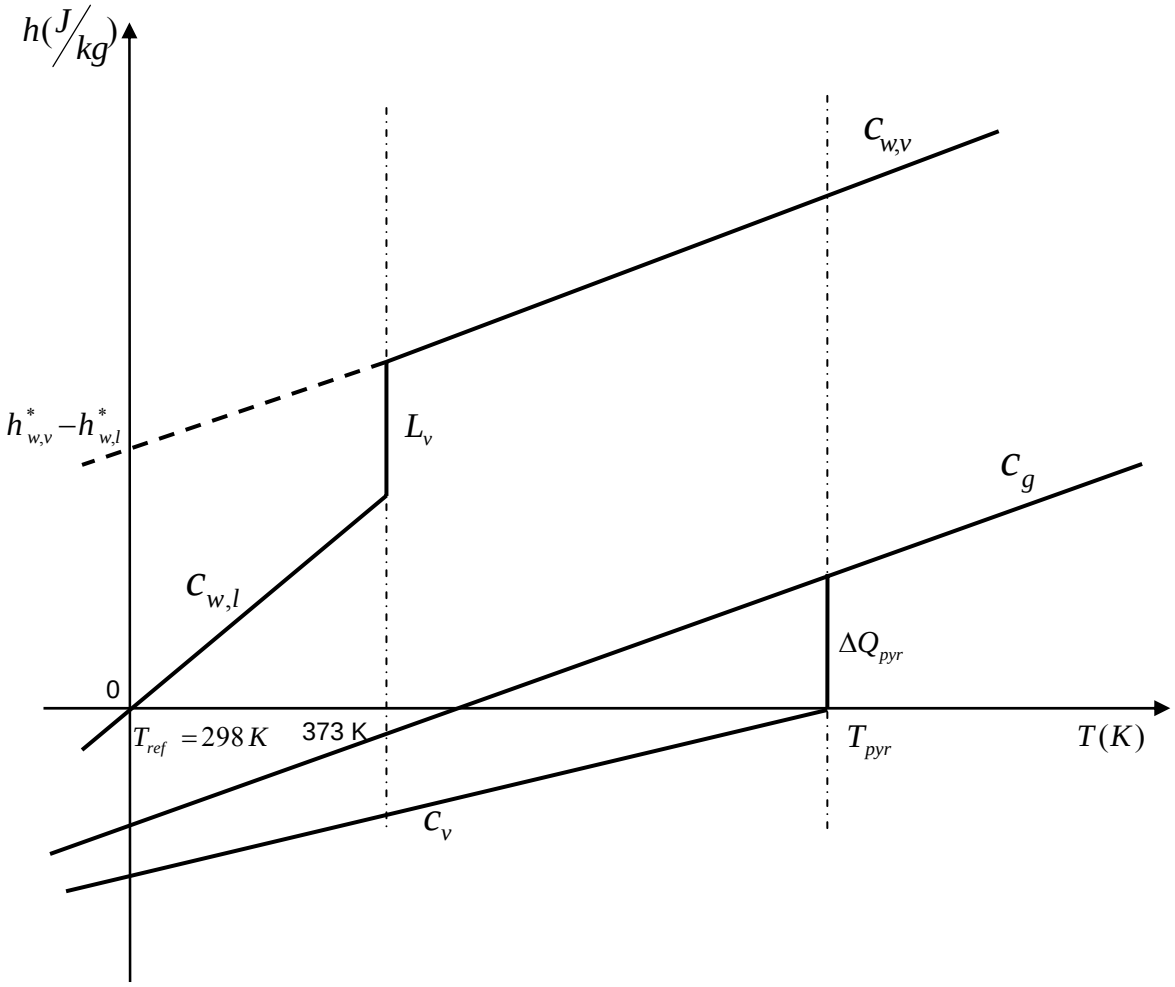

Figure 1. Enthalpy of different constituents as function of temperature for charring materials (top) and non-charring materials (bottom).

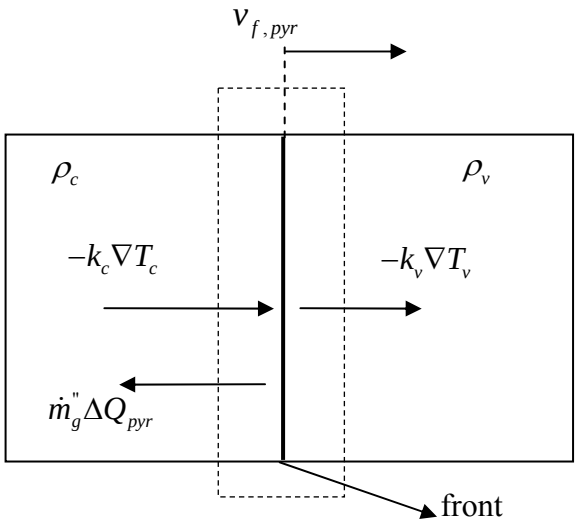

Figure 2. Energy balance at the pyrolysis front.

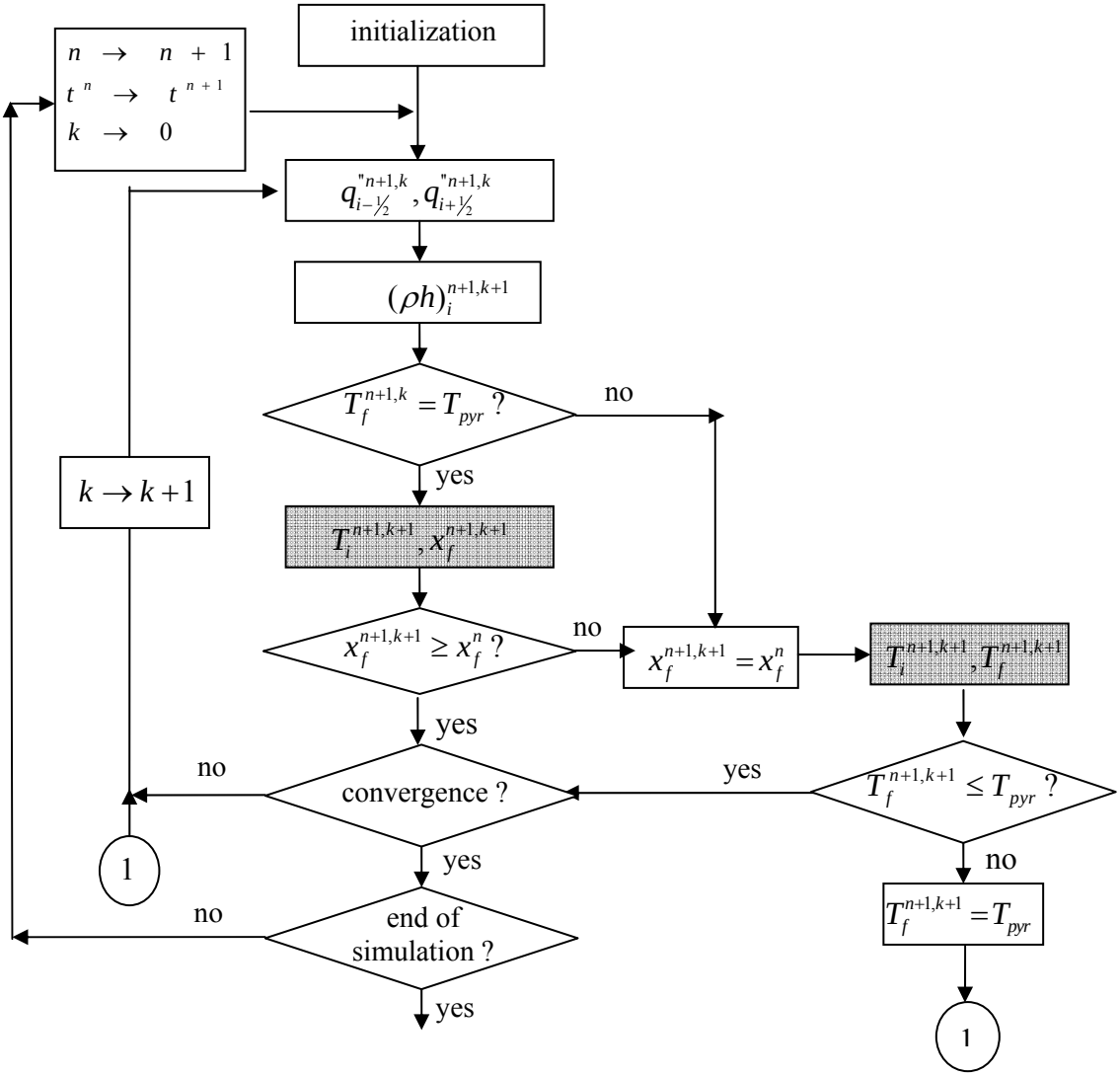

Figure 3: Flow chart: Solution procedure for dry charring materials (mushy cell).

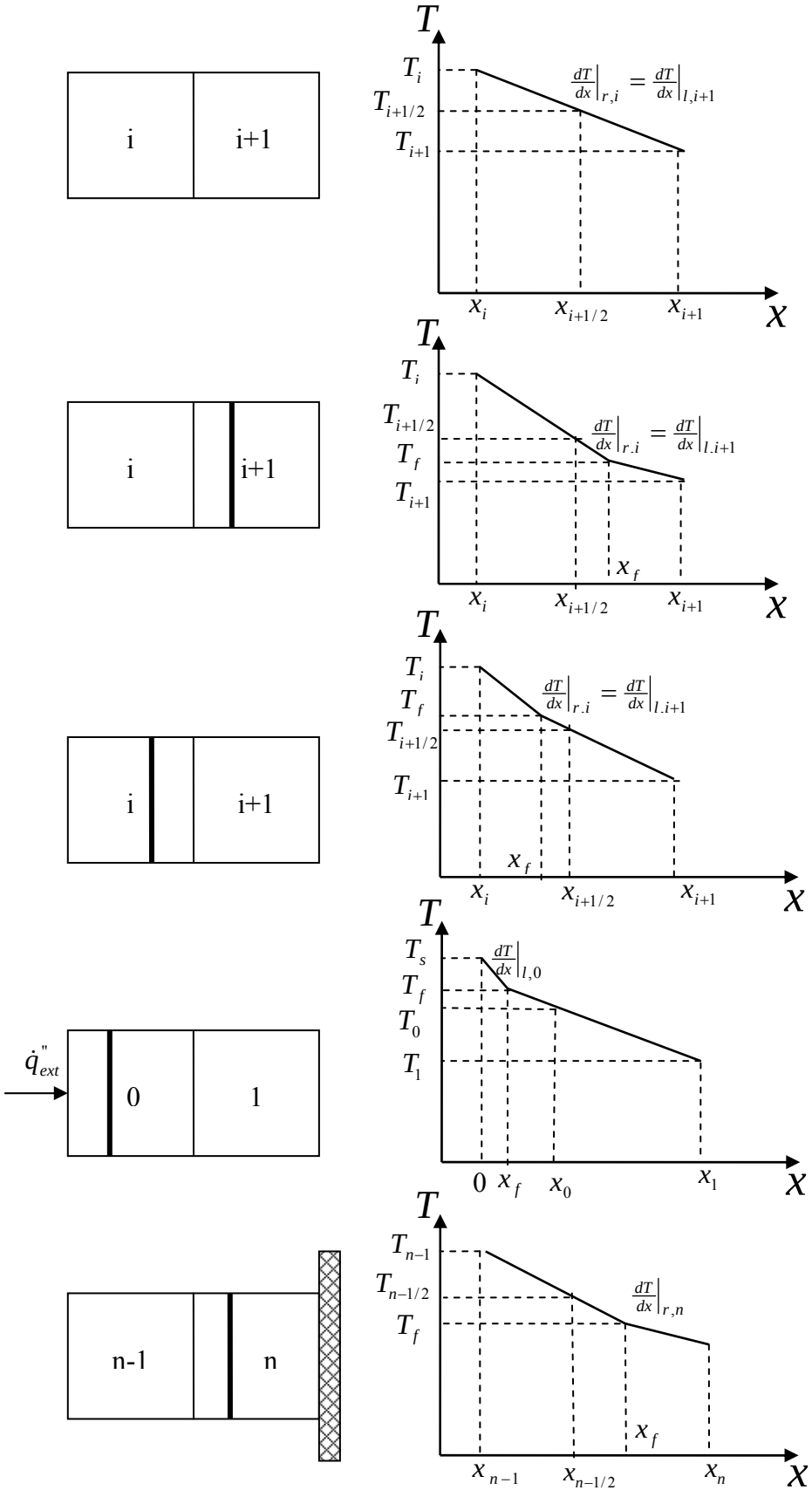

Figure 4: Piecewise linear temperature distribution.

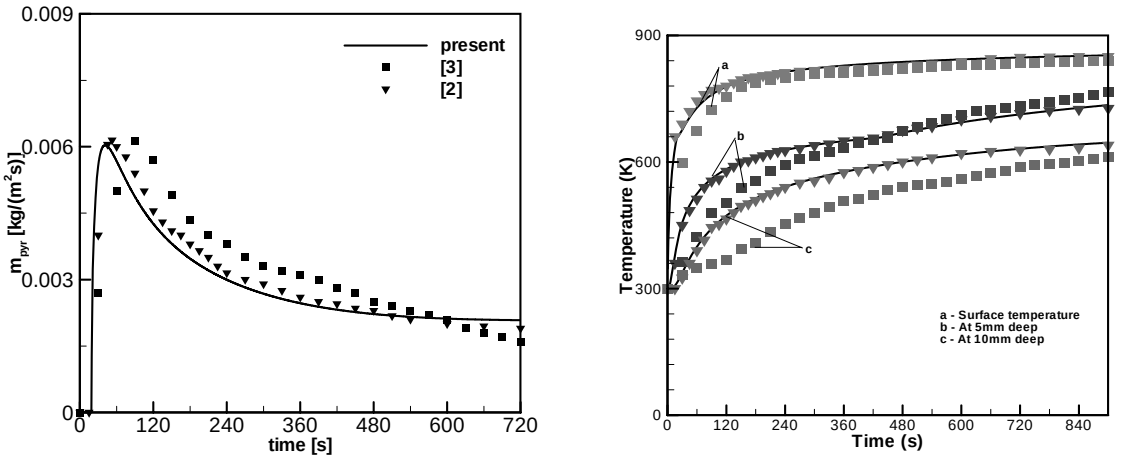

Figure 5. Left: Pyrolysis gases mass flow rate evolution in time. Right: Temperature evolution in time (Depths: surface, 5mm and 10mm). Solid line: numerical simulation. Symbols: squares: experimental data [3]; triangles: numerical results [2].

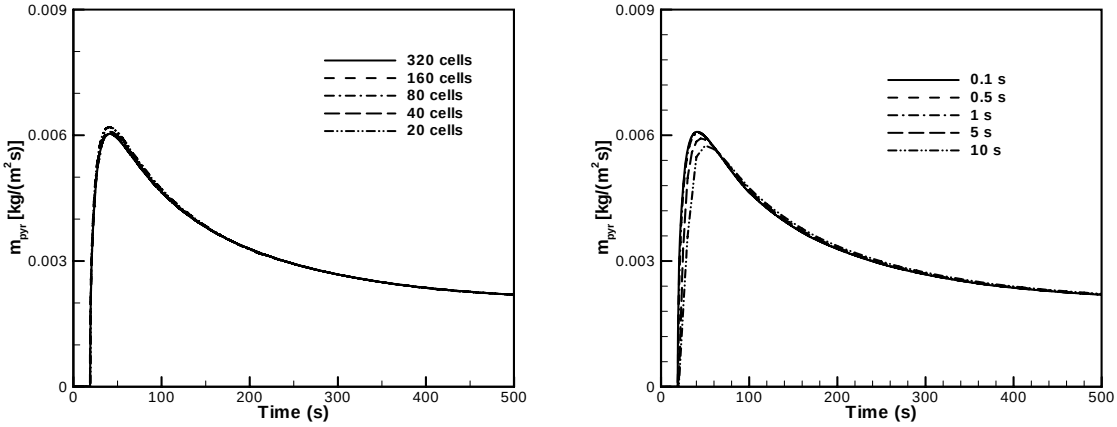

Figure 6. Left: Influence of the number of cells on the evolution of pyrolysis gases mass flow rate in time (physical time step equal to 0.5s). Right: Influence of the physical time step size on the evolution of pyrolysis gases mass flow rate in time (number of cells equal to 40).

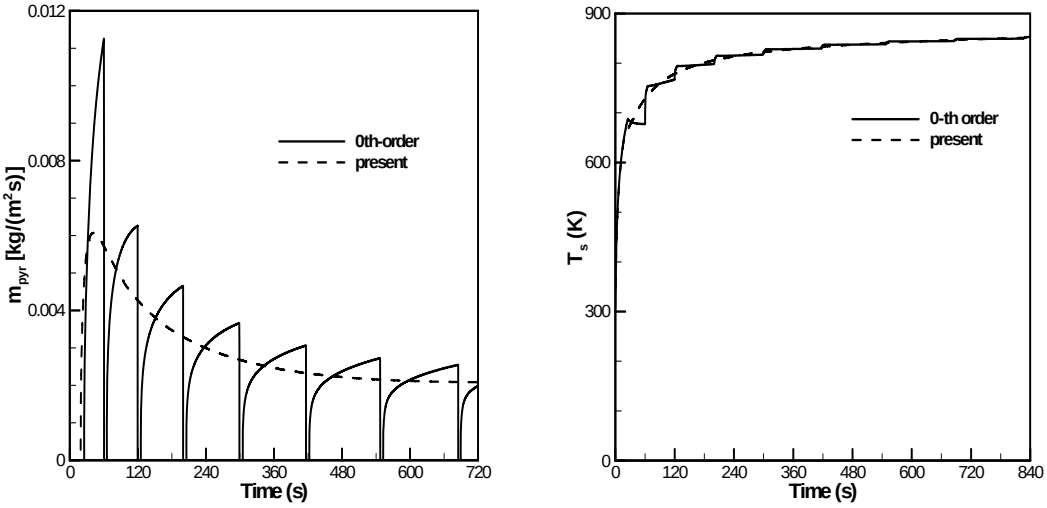

Figure 7: Evolution in time of pyrolysis gases mass flow rate (left) and surface temperature (right). Dashed line: piecewise linear temperature representation; solid line: zero-th order temperature representation.

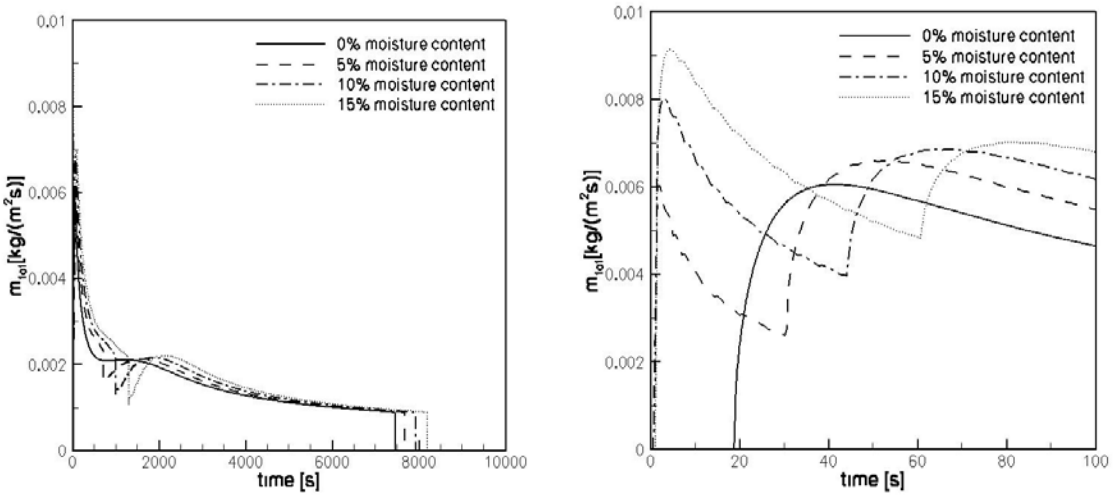

Figure 8. Pyrolysis gases total mass flow rate evolution in time. Right: zoom of the left figure up to 100s.

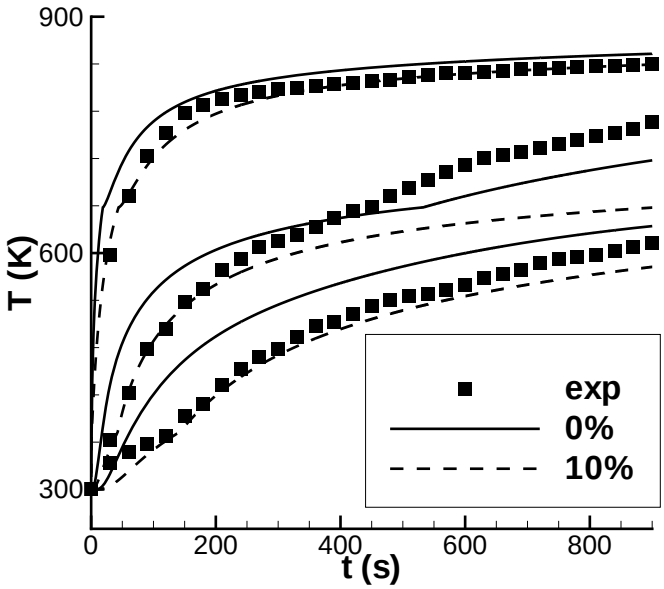

Figure 9. Temperature evolution in time (Depths: surface, 5mm and 10mm). Solid line: dry material; dashed line: 10% moisture content. Squares: experimental data [3].

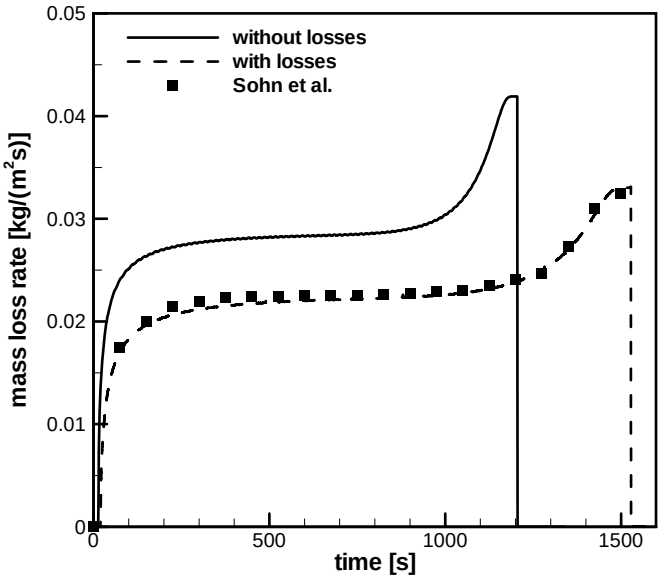

Figure 10. Mass loss rate evolution in time (non-charring material).

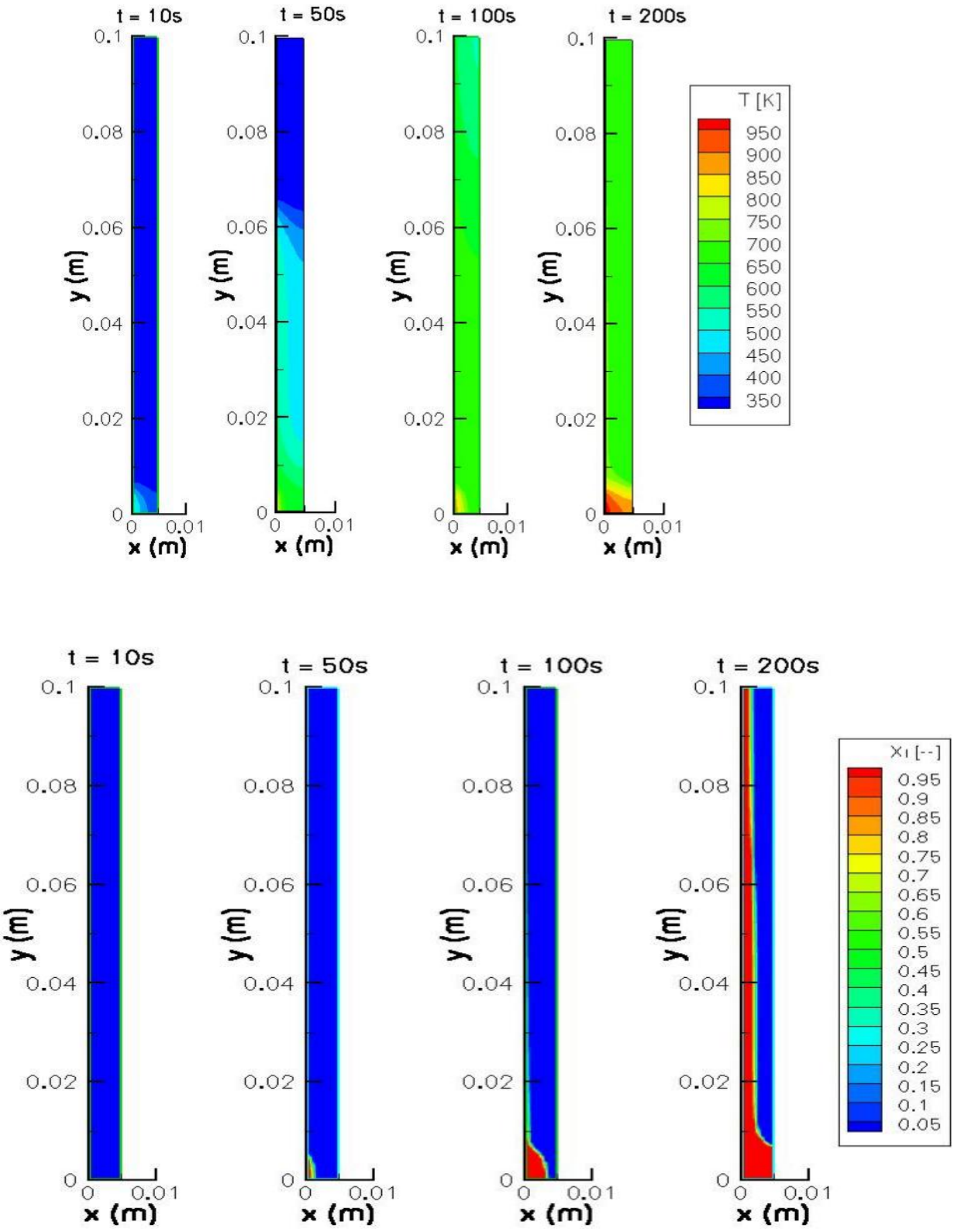

Figure 11. Temperature (top) and char fraction (bottom) fields after 10s, 50s, 100s and 200s.

Material thickness equal to 5mm.

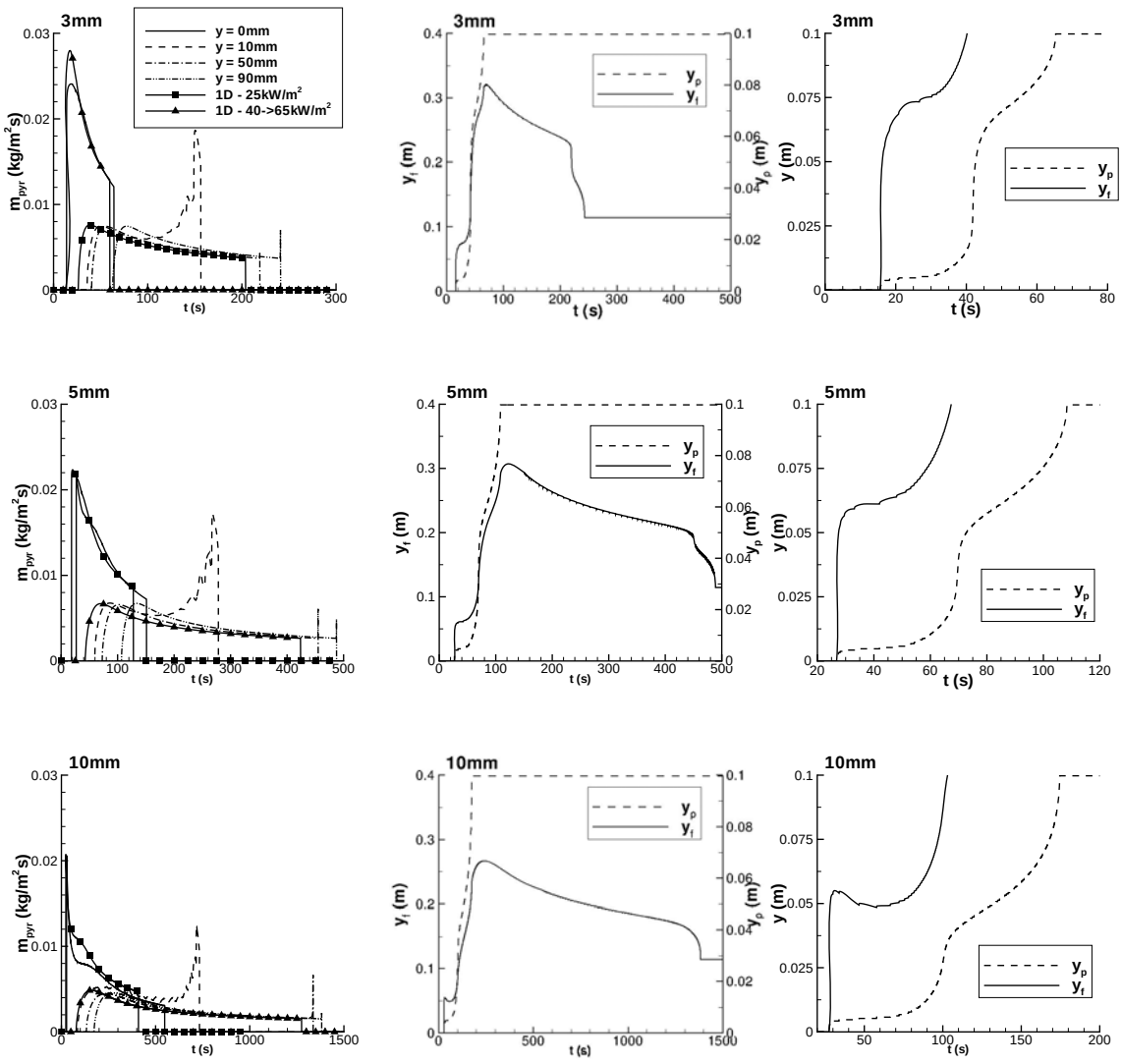

Figure 12. Left: Mass flow rate evolution in time at y = 0mm, y = 1cm, y = 5cm and y = 9cm. Middle: evolution of y_p and y_f; Right: early stages of the evolution of y_p and y_f. Top: thickness = 3mm; middle: thickness = 5mm; bottom: thickness = 10mm. 1D: one-dimensional results for comparison purposes.

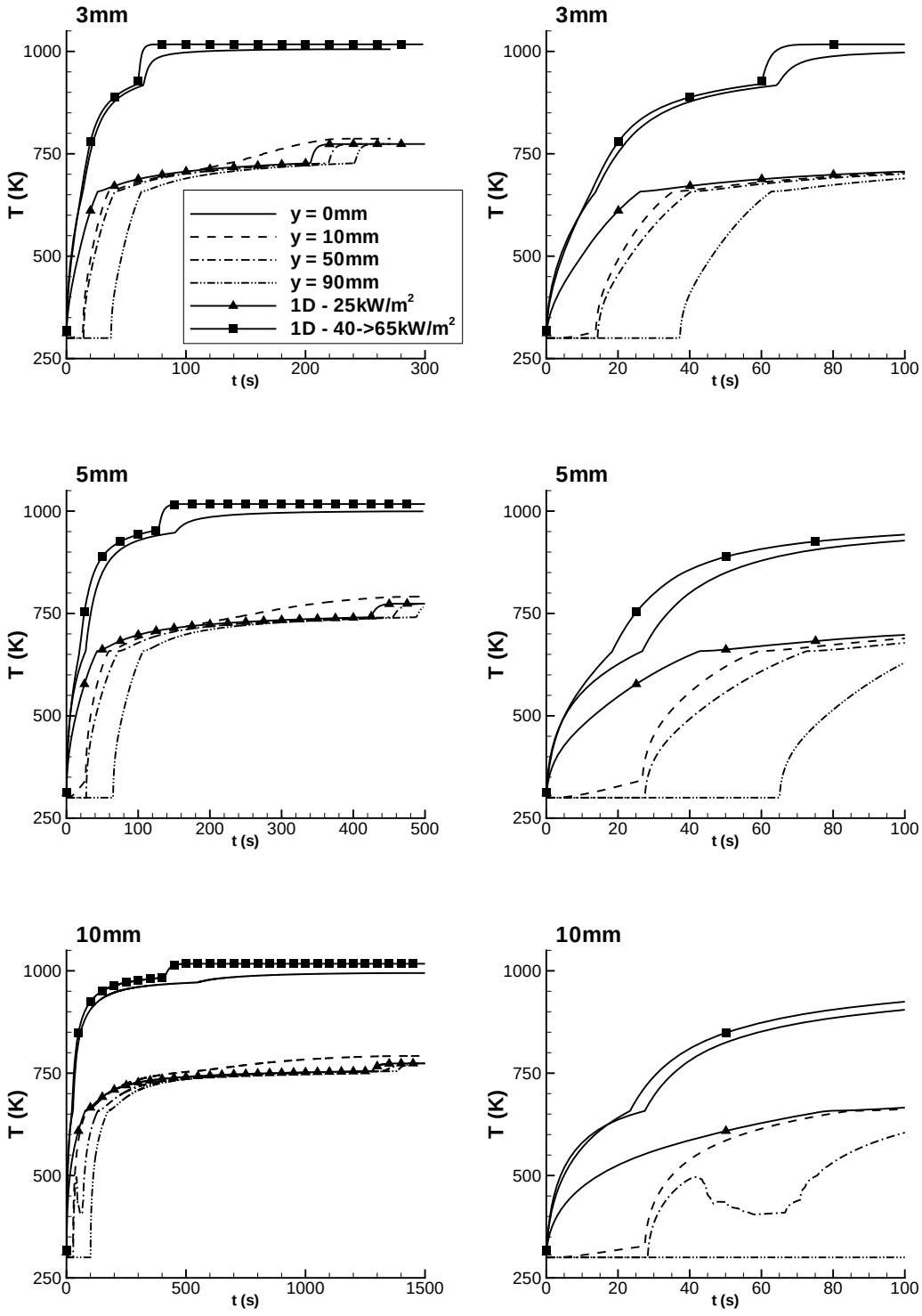

Figure 13. Surface temperature evolution in time at y = 0mm, y = 1cm, y = 5cm and y = 9cm. Top: thickness = 3mm; middle: thickness = 5mm; bottom: thickness = 1cm. 1D: one-dimensional results for comparison purposes.